Author Manuscript

Author Manuscript

Author Manuscript

Author Manuscript

HHS Public Access

Author manuscript

Cell Rep. Author manuscript; available in PMC 2021 August 17.

Published in final edited form as:

Cell Rep. 2021 August 03; 36(5): 109497. doi:10.1016/j.celrep.2021.109497.

Dentate spikes and external control of hippocampal function

Dino Dvorak[1,4], **Ain Chung**[1,3], **Eun Hye Park**[1], **André Antonio Fenton**[1,2,5,*]

[1]Center for Neural Science, New York University, New York, NY 10003, USA

[2]Neuroscience Institute at the NYU Langone Medical Center, New York, NY 10003, USA

[3]Present address: Massachusetts General Hospital, Boston, MA 02114, USA

[4]Present address: Gilgamesh Pharmaceuticals, New York, NY 10003, USA

[5]Lead contact

SUMMARY

Mouse hippocampus CA1 place-cell discharge typically encodes current location, but during slow gamma dominance (SG_{dom}), when SG oscillations (30–50 Hz) dominate mid-frequency gamma oscillations (70–90 Hz) in CA1 local field potentials, CA1 discharge switches to represent distant recollected locations. We report that dentate spike type 2 (DS_M) events initiated by medial entorhinal cortex II (MECII)→ dentate gyrus (DG) inputs promote SG_{dom} and change excitation-inhibition coordinated discharge in DG, CA3, and CA1, whereas type 1 (DS_L) events initiated by lateral entorhinal cortex II (LECII)→DG inputs do not. Just before SG_{dom}, LECII-originating SG oscillations in DG and CA3-originating SG oscillations in CA1 phase and frequency synchronize at the DS_M peak when discharge within DG and CA3 increases to promote excitation-inhibition cofiring within and across the DG→CA3→CA1 pathway. This optimizes discharge for the 5–10 ms DG-to-CA1 neuro-transmission that SG_{dom} initiates. DS_M properties identify extrahippocampal control of SG_{dom} and a cortico-hippocampal mechanism that switches between memory-related modes of information processing.

Graphical abstract

This is an open access article under the CC BY-NC-ND license (http://creativecommons.org/licenses/by-nc-nd/4.0/).

*Correspondence: afenton@nyu.edu.

AUTHOR CONTRIBUTIONS

Conceptualization, D.D. and A.A.F.; methodology, D.D. and A.A.F.; formal analysis, D.D.; investigation, D.D., A.C., and E.H.P.; writing – original draft, D.D. and A.A.F.; writing – review & editing, D.D., A.A.F., A.C., and E.H.P.; visualization, D.D. and A.A.F.; funding acquisition, A.A.F.; supervision, A.A.F.

SUPPLEMENTAL INFORMATION

Supplemental information can be found online at https://doi.org/10.1016/j.celrep.2021.109497.

DECLARATION OF INTERESTS

The authors declare no competing interests.

INCLUSION AND DIVERSITY

We worked to ensure sex balance in the selection of non-human subjects. One or more of the authors of this paper self-identifies as an underrepresented ethnic minority in science. While citing references scientifically relevant for this work, we also actively worked to promote gender balance in our reference list.

Author Manuscript Author Manuscript Author Manuscript Author Manuscript

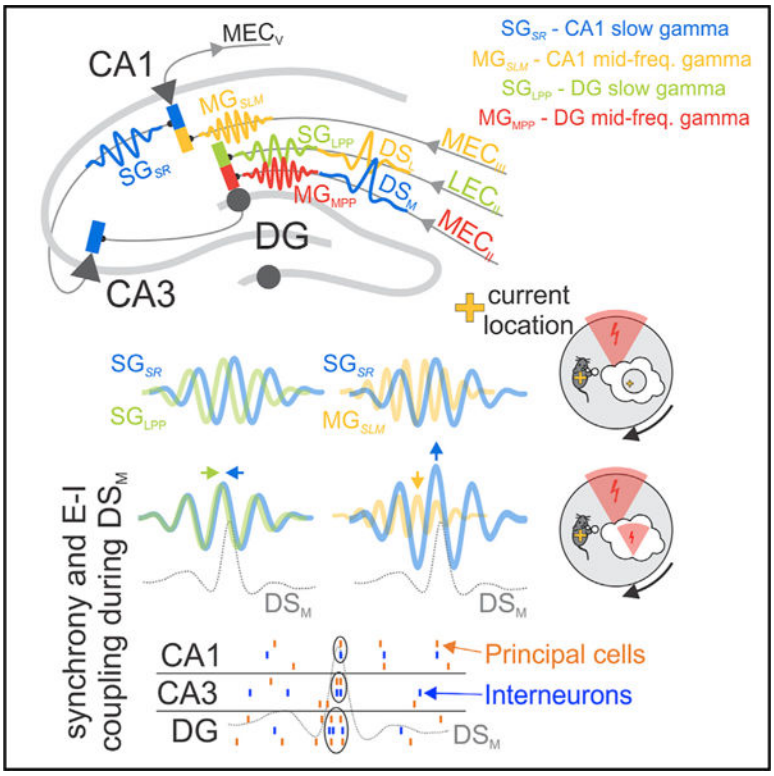

In brief

MECII-originating type 2 dentate spikes (DS_M) promote dominance of CA1 slow (~40-Hz) over mid-frequency (~80-Hz) gamma oscillations when CA1 represents non-local recollections. Dvorak et al. show that DS_M coordinates cofiring within DG, CA3, and CA1 networks and optimizes discharge timing between DG and CA1 for information transfer during memory recall.

INTRODUCTION

The hippocampus is critical for long-term memory storage and use, requiring that neural discharge represents both what has occurred and what is happening. How do multifunction neural networks like the hippocampus accomplish mutually incompatible tasks such as recollecting the past and encoding the present? One possibility is that separate neural circuits operate in parallel to perform each information-processing task, but this does not appear to be the case for the hippocampus. Rather, in the hippocampus, the same populations of excitatory and inhibitory neurons are organized such that network discharge patterns, sometimes called cell assemblies (Harris et al., 2003; Hebb, 1949) rapidly switch between different information-processing modes, often in a winner-take-all fashion during vicarious trial-and-error and other choice behaviors (Colgin, 2015; Johnson and Redish, 2007; Kelemen and Fenton, 2010, 2013, 2016; Papale et al., 2016; Pastalkova et al., 2008; van Dijk and Fenton, 2018; Wu et al., 2017). We first reported variability in the discharge of hippocampus place cells that was so extreme, it was incompatible with these cells merely signaling the current location within a single cognitive map (Fenton and Muller, 1998; Jackson and Redish, 2007; Olypher et al., 2002a, 2002b) and we went on to show that

Author Manuscript Author Manuscript Author Manuscript Author Manuscript

this variability could be explained as multiple spatial representations during tasks with purposeful behaviors that were directed to specific places (Fenton et al., 2010; Kelemen and Fenton, 2010, 2013, 2016). In an alternation task, such variability was organized as place representations that alternate within sequences of ~8-Hz theta oscillations, perhaps reflecting planning between which upcoming alternatives to choose (Kay et al., 2020). We previously reported that position-representing CA1 ensemble spike trains switch between representing the current, local position and distant specific places, which during an active place-avoidance task represented recollected locations of prior foot shock (Dvorak et al., 2018). Specifically, CA1 discharge switched to signaling distant places during slow gamma dominance (SG_{dom}), when CA1 SG (30–50 Hz) oscillations dominate CA1 mid-frequency (70–90 Hz) gamma oscillations. Now that it is established that such network transitions occur to change hippocampal cognitive information processing, it is essential to understand how such transitions may occur in the hippocampus as well as other cognitive networks that transiently switch information-processing modes in circumstances that are physically unchanged.

RESULTS

SG_{dom} in the CA1 local field potential (LFP) switches CA1 place-signaling discharge to represent recollection of distant locations

Well-trained mice on the rotating place-avoidance arena make evasive movements away from the advancing shock zone, as illustrated in the upper portion of Figure 1A. This behavior demonstrates that the mice recollect locations where they were previously shocked. Approximately 1–2 s before mice run away to avoid the location of the shock, we observe SG_{dom} in the CA1 LFP, which is the result of a relatively increased rate of SG (30–50 Hz) oscillations and a decreased rate of mid-frequency gamma (70–90 Hz) oscillations (Figure 1A, bottom). The likelihood of SG_{dom} is elevated before mice express active avoidance, with the peak 1.75 s before, when the mice are often inactive (Figures 1A and 1B). In contrast, SG_{dom} is unlikely during the passive approach to the shock zone if the mice fail to avoid the approaching shock zone and rather run away to escape after receiving a shock (Figure 1B). Such failed avoidances are rare, and most likely occur because the mice did not recollect the location of the shock. Place cells with firing fields in the vicinity of the shock discharge transiently for ~500 ms during SG_{dom}, despite the mice not being in the vicinity of the shock, which can be seen in a single 5-s example (Figure 1C) and in the group data (Figure 1D), and is confirmed by analysis of place cell overdispersion (Figures S1A–S1D). Conversely, place cell ensemble discharge continues to decode to the current location when mice fail to avoid the shock (Dvorak et al., 2018). Because CA1 ensemble discharge can transiently switch from signaling the current location to signaling a distant, recollected location, we wondered which network mechanisms can cause this switch between information processing modes (Figure 1E).

One way to switch between multiple mutually exclusive tasks is to organize the network so that its intrinsic excitation-inhibition dynamics are so balanced that the network spontaneously transitions between multiple information-processing modes through intrinsic winner-take-all mechanisms (Figures 1E and 1F upper; de Almeida et al., 2009; Rolls and

Author Manuscript Author Manuscript Author Manuscript Author Manuscript

Treves, 1998). In the alternative scenario explored here, SG_{dom}-associated switches of the CA1 information-processing mode are controlled by discrete events in the perforant path trisynaptic input from the entorhinal cortex (EC) (Figure 1F, lower).

Identifying the two types of dentate spike (DS) originating from distinct perforant path inputs

CA1 SG originates in CA3 (Lasztóczi and Klausberger, 2014, 2016; Schomburg et al., 2014), motivating us to seek evidence of extrahippocampal control signals in the perforant path projection from ECII to dentate gyrus (DG). We examine DSs, the underinvestigated, large-amplitude, short-duration field potentials that localize to DG (Figures 2A and S1E). They result from entorhinal activation; DSs disappear after bilateral removal of the EC (Bragin et al., 1995). Similar to sharp-wave ripples (SWRs), DSs are synchronized across hemispheres (Bragin et al., 1995; Headley et al., 2017), but in contrast to SWRs, DSs are thought to cause a synchronized inhibition of granule cells and down-stream CA3 and CA1 networks (Figure 2A, left; Penttonen et al., 1997).

Using current source density (CSD) analysis, we classify two types of DS events (Figure 2B; STAR Methods) as DS_L (current sink in outer molecular layers of DG) and DS_M (current sink in middle molecular layers of DG), corresponding to types 1 and 2 identified in the rat (Bragin et al., 1995) and the mouse (Buzsáki et al., 2003). Localization of the outer and middle molecular layers of DG is confirmed by the average CSD of the evoked response to stimulating the medial perforant path (MPP; Figure 2C, right). The DS_L amplitude is larger than the DS_M (Figure 2D; paired $t_8 = 2.87$, $p = 0.02$), while the DS_M width is greater than the DS_L (paired $t_8 = 8.56$, $p = 10^{-5}$). DS_L before DS_M is more likely than vice versa (Figure 2E; paired $t_8 = 5.61$, $p = 10^{-4}$). The average CSDs of DS_L and DS_M during stillness (speed <2 cm/s) and running (speed >3 cm/s) do not visibly differ (Figure 2F). Rates of DS_L and DS_M events are not different, but they are differentially modulated by speed (Figure 2G; 2-way type × speed $ANOVA_{r.m.}$, type: $F_{1,14} = 0.02$, $p = 0.88$; speed: $F_{3,12} = 5.53$, $p = 0.013$; interaction: $F_{3,12} = 5.26$, $p = 0.015$, post hoc tests: $DS_M > DS_L$ at the greatest speeds of 6–8 cm/s). DS_L and DS_M are distinct in origin and morphology but are not independent and are modulated by behavior, and DS_M is more likely to follow DS_L.

DSs modulate oscillatory activity in CA1

We investigate whether DS_L and DS_M influence the CA1 oscillatory activity components of SG_{dom}. Analysis of CA1 oscillatory dynamics using LFP spectral power is confounded by the spectral leakage of DS events in the 30- to 50-Hz range (Figure 3A). Accordingly, we use independent component analysis (ICA; STAR Methods), which identifies two ICs in the CA1 LFP below 100 Hz (Figure 3B), a CA3-originating, *stratum radiatum*-localized SG IC (SG_{SR}; mean frequency 34.1 ± 3.0 Hz; Figures 3C, left, and S2A) and a medial ECIII (MECIII)-originating, *stratum lacunosum moleculare*-localized mid-frequency gamma IC (MG_{SLM}; mean frequency 68.9 ± 3.4 Hz; Figures 3C, right, and S2A).

If DSs modulate CA1 oscillatory activity, then they should systematically co-occur with SG_{SR} and MG_{SLM} oscillatory events. SG_{SR} oscillatory events occur close to the theta trough (339.2° ± 71.4°), whereas the MG_{SLM} oscillatory events occur close to the theta peak

Author Manuscript Author Manuscript Author Manuscript Author Manuscript

(220.5° ± 59.9°; Figure 3D, top), in agreement with prior work (Fernández-Ruiz et al., 2017; Lasztóczi and Klausberger, 2014). DS_M events occur at the theta trough, coinciding with SG_{SR} oscillatory events (344.0° ± 59.8°; Watson-Williams multi-sample test $F_{1,15} = 0.19$, $p = 0.67$), whereas the DS_L events occur close to the theta peak, coinciding with the MG_{SLM} oscillatory events (233.6° ± 71.2°; Watson-Williams multi-sample test $F_{1,15} = 3.48$, $p = 0.08$; Figure 3D).

The theta phase alignment of DS_L and MG_{SLM} events and the distinct phase alignment of DS_M and SG_{SR} events may be expected if DS events control CA1 gamma events, motivating us to determine whether DS events also influence locally generated CA1 gamma power. We compute DS_L- and DS_M-triggered IC power profiles by averaging the Z-scored wavelet spectrogram computed from identified ICs across 25–45 Hz for SG_{SR} and 45–85 Hz for MG_{SLM} (Figure 3E). To evaluate whether the potential influence of the DS events on the CA1 ICs is distinct from the theta modulation of IC power (see Figure 3D), we also compare control power profiles triggered by random events that have the same theta phase distribution as the corresponding DS events, but only a chance association with the DS events. Data from 8 of 9 mice are analyzed because 1 mouse did not have CA1 electrode coverage. MG_{SLM} is increased 36% at the DS_L peak compared to random (paired $t_7 = 6.82$, $p = 10^{-4}$), while SG_{SR} is not (paired $t_7 = 0.35$, $p = 0.7$; Figure 3E, left). In contrast, SG_{SR} is increased 67% at the peak of DS_M compared to random (paired $t_7 = 5.0$, $p = 0.002$), while MG_{SLM} is decreased during DS_M (paired $t_7 = 2.68$, $p = 0.03$; Figure 3E, right).

To examine the co-occurrence of the DS and CA1 gamma oscillatory events, we randomly pick 1,000 times from each 30-min recording and assess whether MG_{SLM} or SG_{SR} occurs within a 50-ms coincidence interval of DS_L or DS_M. The probability of observing SG_{SR} is greater if DS_M is observed (Figure 3F, left; $F_{3,31} = 9.59$, $p = 10^{-4}$, $p(SG_{SR} \mid DS_M) > p(SG_{SR} \mid DS_L) = p(SG_{SR} \mid nonDS_M) = p(SG_{SR} \mid nonDS_L)$), while the probability of observing MG_{SLM} is greater if a DS_L event is observed (Figure 3F, right; $F_{3,31} = 7.31$, $p = 10^{-4}$, $p(MG_{SLM} \mid DS_L) > p(MG_{SLM} \mid DS_M) = p(MG_{SLM} \mid nonDS_L) = p(MG_{SLM} \mid nonDS_M)$).

Since DS_M increases the power of CA3-originating SG_{SR} (Figure 3E) and DSs co-occur with CA3-originating SWRs (Bragin et al., 1995), we computed the probability of a SWR within ±50 ms of DS_L, DS_M, and random events during stillness (speed <2 cm/s; Figure 3G). SWR probability is increased ±10 ms of the DS_M peak, but not DS_L (Figure 3G; 1 sample test for proportions: $p(SWR \mid DS_L) = 0.012$, $Z = 0.71$, $p = 0.3$; $p(SWR \mid DS_M) = 0.018$, $Z = 13.20$, $p = 10^{-39}$).

If DS_M controls the CA1 information-processing mode, these findings of DS modulation of CA1 gamma predict that DS_M (but not DS_L) promotes CA1 SG_{dom}. We evaluated this prediction using SG_{dom} events collected during place-avoidance behavior, in which SG_{dom} events identify recollection (Figure 1). The rate of DS_M but not DS_L events is elevated at the time of SG_{dom} (Figure 3H; DS_L: $t_{5,255} = 1.81$, $p = 0.07$; DS_M: $t_{5,255} = 5.07$, $p < 0.0001$).

DSs modulate individual cycles of CA1 gamma oscillations, DS_M promoting SG_{dom}

If DS_M events control CA1 information processing by promoting SG_{dom}, then DS_M should influence CA1 gamma oscillations with a precision comparable to the ~6-ms conduction

Author Manuscript Author Manuscript Author Manuscript Author Manuscript

time from the DG to CA1 (Figure 2C, white arrows). Because measuring gamma power requires ~100 ms (3–5 cycles of an oscillatory burst; Figures 3E and S2C), and spiking is most likely during oscillatory minima (Figure S2B; Dvorak and Fenton, 2014; Lasztóczi and Klausberger, 2016; Schomburg et al., 2012), we measure discrete oscillatory events with ~15 ms resolution, as the local minima of oscillatory bursts (Figure 4A, inset; STAR Methods). The findings in Figure 4, data acquired during the place-avoidance task, are essentially similar in home-cage data (Figure S3A).

The probability of observing a MG_{SLM} oscillatory cycle is strongly enhanced ±10 ms of the DS_L peak (paired $t_7 = 5.43$, $p = 0.001$; Figure 4A, left), as well as 15 ms before and 16 ms after the DS_L peak, corresponding to a MG_{SLM} oscillatory frequency of 69 Hz, whereas the probability of observing a SG_{SR} oscillatory cycle remains unchanged during DS_L (paired $t_7 = 0.69$, $p = 0.52$; Figure 4A, left). In contrast, the probability of observing a SG_{SR} oscillatory cycle is enhanced 6 ms after the peak of DS_M, corresponding to the transmission time between DG and CA1, which is primarily influenced by the CA3→CA1 synaptic delay (Mizuseki et al., 2012; Figure 4A, right; paired $t_7 = 4.52$, $p = 0.003$). The probability of a SG_{SR} oscillatory cycle is also enhanced 24 ms before and 33 ms after the DS_M peak corresponding to a SG_{SR} oscillatory frequency of 34 Hz, whereas the probability of observing a MG_{SLM} oscillatory cycle is not different (Figure 4A right; paired $t_7 = 0.79$, $p = 0.45$;). There is a non-oscillatory increase in the MG_{SLM} oscillatory cycle probability 30–50 ms before DS_M (Figure 4A, right; paired $t_7 = 3.80$, $p = 0.007$) and a reduced probability of observing a MG_{SLM} oscillatory cycle 30–50 ms after DS_M (Figure 4A, right; paired $t_7 = 7.39$, $p = 10^{-4}$).

The consequences of MPP manipulations are not straightforward (Brun et al., 2002; Garner et al., 2012; Kanter et al., 2017; Miao et al., 2015; Schlesiger et al., 2018), which was confirmed by chemogenetic silencing, electrical stimulation of MPP, and anesthesia (Figure S4). Consequently, to rigorously test the hypothesis that DS_M promotes SG_{dom}, we examine whether spontaneously strong and weak DS_M events differentially promote SG_{dom}. Because DS_M can both increase the likelihood of SG_{SR} and attenuate the likelihood of MG_{SLM} to promote SG_{dom}, DS_Ms were classified according to their prominence (Figure 4B), and independently, by the ~10-ms post-DS_M CSD source that suggests increased inhibition, corresponds to the DG→CA1 transmission time, and localizes to the vicinity of the hippocampal fissure and CA1 *slm* (red rectangle in Figure 4B). Because the *slm* CSD source accounts for only 8% of the variance in DS_M prominence (Figures 4C and 4D; $r^2 = 0.084$, $p < 0.0001$), we used both features to evaluate the causal predictions that (1) DS_M events with a large prominence will increase SG_{SR} and (2) that DS_M events with a large *slm* CSD source will decrease MG_{SLM}, each promoting SG_{dom}.

The probability of observing SG_{SR} and MG_{SLM} oscillatory cycles was computed in relation to the 10% of DS_M with the highest and lowest prominence DURING ±10 ms of the DS_M peak (orange bar in Figure 4E), 30–50 ms BEFORE (green bar in Figure 4E), and 30–50 ms AFTER (magenta bar in Figure 4E). CA1 SG_{SR} oscillatory cycles were more likely DURING ($F_{2,17} = 13.10$, $p = 0.0005$, high > low = random) and AFTER ($F_{2,17} = 12.15$, $p = 0.0007$, high > low = random) the high prominence DS_M events compared to the low prominence DS_M and random events. These patterns were not observed in relation to DS_L

Author Manuscript Author Manuscript Author Manuscript Author Manuscript

events (Figure S3C). CA1 SG_{SR} oscillatory cycles were most probable ~10 ms after the high and low prominence DS_M peaks, similar to the DG →CA1 transmission time. In contrast, CA1 MG_{SLM} oscillatory cycles were more likely BEFORE high prominence DS_M ($F_{2,17}$ = 8.32, p = 0.004, high > low = random) but not AFTER ($F_{2,17}$ = 2.73, p = 0.09). Both the high and low prominence DS_L events increased the probability of MG_{SLM} oscillatory cycles during DS_L (Figure S3D). These findings further support the hypothesis that DS_M controls SG_{SR} to promote SG_{dom} in CA1.

Complementary patterns of promoting SG_{dom} are evident when DS_M events are categorized as being the 10% with the largest or smallest *slm* CSD source (Figure 4F). CA1 MG_{SLM} oscillatory cycles were more likely BEFORE ($F_{2,17}$ = 9.57, p = 0.002, large > small = random) and less likely DURING ($F_{2,17}$ = 16.93, p = 0.0001, small > large = random) and AFTER ($F_{2,17}$ = 20.68, p < 0.0001, small > random > large) DS_M events with large *slm* CSD sources (Figure 4F, right). CA1 SG_{SR} oscillatory cycles were less likely BEFORE ($F_{2,17}$ = 5.39, p = 0.017, small > large = random), DURING ($F_{2,17}$ = 11.42, p = 0.001, small > large > random), and AFTER ($F_{2,17}$ = 7.00, p = 0.0071, small > large > random) DS_M events with large *slm* CSD sources (Figure 4F, left). These analyses confirm the causal predictions that the prominence of DS_M and the amplitude of the associated *slm* CSD source together control SG_{SR} and MG_{SLM} gamma oscillations to promote SG_{dom}.

DS_M synchronizes DG and CA1 SG band oscillations

Dentate DS_M events increase CA3-originating SG_{SR} to promote SG_{dom}, but is CA3 activity under enhanced or reduced DG influence during DS_M? We start by studying the synchrony of DG and CA1 oscillations during DS_L and DS_M. ICA combined with CSD-based classification of DS events disentangles DS events and DG oscillatory components that both originate in the perforant path projection to DG (Figures S2D–S2M; Barth et al., 2018; Fernández-Ruiz et al., 2013; McNaughton, 1980). ICA identified a lateral perforant path (LPP) IC localized to the outer molecular layer DG sinks in the CSD (Figure S2M) of the ICA voltage loadings and has a SG peak in the CA1 theta phase comodulogram (SG_{LPP}; Figure 5A, bottom left; mean frequency 43.9 ± 5.0 Hz). The MPP IC (Figure 5A, right) localized to the middle molecular layer DG sinks in the CSD (Figure S2M) of the ICA voltage loadings and has a mid-frequency gamma peak in the CA1 theta phase comodulogram (MG_{MPP}; Figure 5A, bottom right; mean frequency 71.0 ± 2.7 Hz). While the mean frequency of dentate SG_{LPP} is higher than the mean frequency of the CA1 SG_{SR} (paired t_6 = 3.69, p = 0.01), the mean frequencies of dentate MG_{MPP} and CA1 MG_{SLM} do not differ (paired t_6 = 2.17, p = 0.07).

CA1 theta is used as an intrinsic network time reference to analyze the phase preference of the dentate SG_{LPP} and MG_{MPP} oscillations (Figure 5B). Dentate SG_{LPP} oscillations occur at a late descending phase, close to the theta trough (277.4° ± 74.3°) that precedes both DS_M (Watson-Williams multi-sample test $F_{1,14}$ = 6.3, p = 0.03) and SG_{SR} (Watson-Williams multi-sample test $F_{1,14}$ = 4.5, p = 0.05); compare to Figure 3D. Dentate MG_{MPP} oscillations occur close to the theta peak (214.9° ± 59.8°), similar to DS_L (Watson-Williams multi-sample test $F_{1,14}$ = 1.9, p = 0.19) as well as CA1 MG_{SLM} oscillations (Watson-Williams multi-sample test $F_{1,14}$ = 0.04, p = 0.83); compare to Figure 3D.

Author Manuscript Author Manuscript Author Manuscript Author Manuscript

Because the DG SG_{LPP} and the CA1 SG_{SR} oscillations appear at similar phases of the CA1 theta cycle, and the DG MG_{MPP} and CA1 MG_{SLM} also appear at similar phases of CA1 theta (Figures 3D and 5B), DSs could synchronize the DG and CA1 subfields. We test this possibility by measuring the phase coupling between DG and CA1 SG and mid-frequency gamma oscillations. The frequency-band specific phase locking values (PLVs; Lachaux et al., 1999) time locked to DS events (Figure 5C; STAR Methods) show that the SG_{LPP} and SG_{SR} oscillations are not coupled during DS_L (Figure 5C, top left), whereas MG_{MPP} and MG_{SLM} couple during DS_L (Figure 5C, bottom left). In contrast, the SG_{LPP} and SG_{SR} couple strongly after the DS_M peak (Figure 5C, top right), and MG_{MPP} and MG_{SLM} couple ~50 ms before and ~75 ms after DS_M (Figure 5C, bottom right). The phase interactions are frequency specific, especially in the case of the DS_M-triggered events. Consequently, PLV was averaged across SG 25–45 Hz and mid-frequency 45–85 Hz gamma bands (Figure 5D), and to evaluate whether any DS-related phase coupling between the DG and CA1 gamma oscillations is simply a result of the co-occurrence of DS events and gamma oscillations at similar theta phases (Figures 3D and 5B), we also compute PLV around randomly selected time points that are sampled from the theta phase distributions of the DS_L and DS_M events (gray profiles in Figure 5D). The only significant departure from random was during DS_M, between the SG_{LPP} and the SG_{SR} oscillations (Figure 5D, top right; paired $t_6 = 4.04$, $p = 0.006$). The peak of this phase locking occurs 9 ms after the DS_M peak. Similarly, the DS_M-locked SG_{SR} oscillatory cycles lag behind the SG_{LPP} oscillatory cycles by 6 ms (Figures S3A and S3B), pointing again to the DG→CA1 transmission time that was observed in Figures 2C and 4B.

CA1 SG_{SR} and DG SG_{LPP} are frequency and phase tuned during DS_M

Given a fixed duration of the gamma-generating $GABA_A$ receptor response, the frequency of a gamma oscillation can be adjusted by changing the level of network excitation, such that greater excitation produces faster oscillations because GABA inhibition can be overcome sooner (Whittington et al., 1995). Because the 44-Hz SG_{LPP} and the 34-Hz SG_{SR} oscillate at different frequencies (Figures 3C and 5A), but phase lock during DS_M (Figure 5D), the gamma-generating mechanism predicts input-driven changes in both the frequency and phase relationships for the phase alignment during DS_M. We analyze the frequency relationships of SG_{LPP} and SG_{SR} during DS_M to test the predictions. During DS_M, the frequency of SG_{LPP} decreases from 43 to 36 Hz at the peak of DS_M, whereas the frequency of SG_{SR} increases from 28 to 36 Hz at the peak of DS_M, effectively aligning the frequencies of the DG and CA1 originating oscillations (Figure 5E). Analysis of the phase relationships of SG_{LPP} and SG_{SR} during DS_M (Figure 5F) shows that the maximum deviation from the mean phase difference occurs 25 ms before the DS_M peak ($t_6 = 4.51$, $p = 0.004$) and the phase offset reverts to the mean phase difference by 60 ms after the DS_M peak ($t_6 = 2.37$, $p = 0.06$). At the peak of DS_M, the phase difference is reduced by 14.5° ± 12.8° (from 11 to 9 ms), similar to the DG→CA1 transmission time observed in Figures 2C, 4B, 5D, and S3A.

DS_M increases DG, CA3, and CA1 discharge rates and cofiring

The hypothesis that DS_M has a causal role in promoting SG_{dom} (Figures 3 and 4) and synchronizing SG oscillations at the LPP terminals in DG and CA3 terminals in CA1 (Figure 5) predicts that DS_M organizes DG, CA3, and CA1 discharge. Objectively classified,

Author Manuscript Author Manuscript Author Manuscript Author Manuscript

presumptive principal cells (Es) and narrow waveform interneurons (INs) were localized and studied to test the prediction (Figures 6A and 6B; STAR Methods). We compute the firing rates of presumptive granule cells (GCs, n = 141), mossy cells (MCs, n = 140), CA3 (n = 104), and CA1 (n = 145) Es as well as INs detected in their proximity (n = 435) during 10-ms windows shifted relative to DS_L and DS_M events (Figure 6C). These are compared with the firing rates at random times. DS events contaminated by SWR events were excluded to minimize potential SWR bias (Figure 3G). During DS_L the discharge of GC decreases by 13% ($t_{140} = 2.92$, $p = 0.004$). Similarly, the discharge of MC decreases by 19% ($t_{139} = 3.54$, $p = 0.0005$). CA3 and CA1 Es did not change firing rates (Figure 6C; CA3: $t_{103} = 1.36$, $p = 0.18$; CA1: $t_{144} = 1.49$, $p = 0.14$). In contrast, during DS_M, GC rates increase by 106%, MC rates increase by 117%, and CA3 rates increase by 47%, whereas CA1 E rates do not significantly increase as observed during SG_{dom} (Figure 6C; GC: $t_{140} = 5.82$, $p = 10^{-8}$; MC: $t_{139} = 6.15$, $p = 10^{-9}$; CA3: $t_{103} = 3.02$, $p = 0.003$; CA1: $t_{144} = 1.65$, $p = 0.1$). During DS_L, the discharge of GC-associated (n = 96) and MC-associated (n = 89) INs reduces by 10% and 8%, respectively (Figure 6C; GC IN: $t_{95} = 2.65$, $p = 0.009$; MC IN: $t_{88} = 2.00$, $p = 0.05$), while discharge of CA3-associated (n = 102) and CA1-associated (n = 148) INs increases by 16% and 9%, respectively (Figure 6C; CA3 IN: $t_{101} = 3.72$, $p = 0.0003$; CA1 IN: $t_{147} = 2.40$, $p = 0.017$). In contrast, during DS_M, firing rates of GC-, MC-, CA3-, and CA1-associated INs increase by 263%, 58%, 71%, and 25%, respectively (Figure 6C; GC IN: $t_{95} = 9.51$, $p = 10^{-15}$; MC IN: $t_{88} = 3.41$, $p = 0.0009$; CA3 IN: $t_{101} = 6.28$, $p = 10^{-9}$; CA1 IN: $t_{147} = 4.39$, $p = 10^{-5}$).

These findings suggest that DS_L events result in the net inactivation of both excitatory and inhibitory cells in the DG and the weak activation of INs in CA3 and CA1, without changing the firing rates of CA3 and CA1 Es, whereas DS_M events result in strong activation of both excitatory and inhibitory cells along the DG→CA3→CA1 trisynaptic pathway, with the primary effect in CA1 being to activate presumptive INs. The DS_M-associated increase in both excitatory and inhibitory cells establishes conditions for enhanced temporal control of E discharge through excitation-inhibition coordination, and enhanced opportunities for cofiring that can enhance neural transmission across the DG→CA3→CA1 trisynaptic pathway (Ashhad and Feldman, 2020; Renart et al., 2010).

The hypothesis that DS_M promotes SG_{dom} by increasing neural control via CA3 predicts increased excitatory-inhibitory cofiring during DS_M (Ashhad and Feldman, 2020; Renart et al., 2010), as does a recent finding of increased cofiring between excitatory and inhibitory dentate cell pairs during moments of active and successful discriminative memory recall (van Dijk and Fenton, 2018). We analyze the cofiring of pairs of Es and INs within ±3 ms of DS_L, DS_M, and random events (Figure 6D; Table S1); DS events contaminated by SWR events were excluded. During DS_M, cofiring among the GC and associated IN populations increases relative to chance (Figure 6D, left; 649% ± 734%, $t_{464} = 11.23$, $p = 10^{-26}$), whereas the cofiring decreases during DS_L (65% ± 108%, $t_{464} = 4.89$, $p = 10^{-6}$). E and IN cofiring also increases during DS_M within CA3 (232% ± 299%, $t_{518} = 7.18$, $p = 10^{-12}$), but does not change during DS_L (88% ± 87%; $t_{518} = 2.26$, $p = 0.02$). Increased cofiring between Es and INs is also observed within CA1 during DS_M (132% ± 137%; $t_{361} = 5.46$, $p = 10^{-7}$), indicating potentially increased inhibitory control of E spiking during DS_M but not during DS_L (105% ± 131%; $t_{361} = 2.83$, p = not significant [n.s.] after Bonferroni correction).

Author Manuscript Author Manuscript Author Manuscript Author Manuscript

Cofiring also increased during DS_M, but not DS_L, between MC- and GC-associated INs (623% ± 676%, $t_{121} = 8.90$, $p = 10^{-15}$) and between CA3- and CA1-associated INs (180% ± 214%, $t_{196} = 5.53$, $p = 10^{-8}$).

These increases in the propensity for cofiring during DS_M imply that local neurotransmission between excitatory and inhibitory cells is enhanced between synaptically coupled cell pairs during DS_M. Enhanced spike-transmission strength estimated from cell pair spike time cross-correlograms has been used to identify monosynaptically (excitatory) coupled cell pairs (Figure 6E; English et al., 2017; Stark and Abeles, 2009). Summary of the types of cell-class pairs identified by enhanced short-latency spike-transmission strength highlights a greater likelihood of detecting intraregional coupling, including via common input, and electrical synapses (review in Traub et al., 2018; Figure 6F), as may be the case for IN-IN cell pairs that exhibit zero-lag coupling. The average cross-correlograms confirm that during DS_M, cofiring is enhanced between excitatory–inhibitory cell pairs that are likely to be monosynaptically connected and possibly involved in rhythmogenesis (Figures 3E, 3F, and 4A) in the DG, CA3, and CA1 (5-ms window; paired t test calculated at maximum cofiring value; GC/E × GC/IN: DS_M: $t_3 = 3.41$, $p = 0.04$; DS_L: $t_3 = 0.71$, $p = 0.53$; CA3/E × CA3/IN: DS_M: $t_{50} = 4.62$, $p = 10^{-5}$; DS_L: $t_{50} = 2.96$, $p = 0.004$; CA1/E × CA1/IN: DS_M: $t_{29} = 4.05$, $p = 0.0003$; DS_L: $t_{29} = 1.43$, $p = 0.16$). Furthermore, cofiring is enhanced during DS_M, but not DS_L, between pairs of granule cells (GC/E × GC/E; DS_M: $t_4 = 5.99$, $p = 0.004$; DS_L: $t_4 = 1.11$, $p = 0.32$), pairs of CA3 INs (CA3/IN × CA3/IN; DS_M: $t_{13} = 4.49$, $p = 0.0006$; DS_L: $t_{13} = 0.37$, $p = 0.72$), and pairs of CA1 INs (CA1/IN × CA1/IN; DS_M: $t_9 = 3.68$, $p = 0.005$; DS_L: $t_9 = 1.61$, $p = 0.14$). DS_M selectively activates local excitation-inhibition network discharge in both DG and CA3, which control neuron cofiring between the DG and CA3 networks, likely to promote SG_{dom} and increase excitation-inhibition discharge in CA1.

Finally, because DS_M promotes the synchronization of SG_{SR} and SG_{LPP} in the SG frequency range (Figures 5C–5F), neuronal discharge (Figure 6C), and cofiring (Figures 6D, G) within the DG-CA3-CA1 networks, it predicts that the DS_M-enhanced SG_{SR} rhythm orchestrates the discharge through spike-field coupling that can maximize the efficiency of information transfer from DG to CA1. To evaluate this hypothesis, we examine the SG_{SR} and SG_{LPP} spike-field coupling during DS events (Figure 7). The spiking of DG cells, CA3, and CA1 Es is more organized at the trough of SG_{SR} oscillations in CA1 during DS_M compared to DS_L (Figures 7A–7C; Kuiper test comparing the DS_L- and DS_M-associated discharge probability distributions across SG_{SR} phase at the time of the DS peak; GC/E: $k = 1{,}652$, $p = 0.001$; CA3/E: $k = 465$, $p = 0.02$; CA1/E: $k = 836$, $p = 0.01$). In contrast, at the time of DS_M, SG_{LPP} oscillations organize the local spiking of dentate GCs but not CA3 and CA1 Es when compared to DS_L (Figures 7D–7F; GC/E: $k = 1{,}508$, $p = 0.001$; CA3/E: $k = 374$, $p = 1$; CA1/E: $k = 516$, $p = 1$). Similar relationships were observed for INs recorded in the vicinity of DG granule cells and CA3 and CA1 INs (Figure S6). These findings indicate that DS_M synchronizes discharge across the DG-CA3-CA1 trisynaptic circuit to SG_{SR}, which enhances DG-CA1 transmission and promotes SG_{dom}.

Author Manuscript Author Manuscript Author Manuscript Author Manuscript

DISCUSSION

DS_M control of information processing in Ammon's horn

Our findings demonstrate entorhinal cortical control of information processing in the hippocampus mediated by DS_M, the result of the synchronous activation of MPP terminals at the middle molecular layer of the DG (Figure 2; Bragin et al., 1995). The effects of DS_M on the DG→CA3→CA1 network are in dramatic and consistent contrast to the effects of DS_L (Figures 3, 4, 5, 6, and 7), making it essential to distinguish them. Conclusions based on work that did not discriminate DS_L from DS_M have been hard to interpret (Bramham, 1998; Nokia et al., 2017). We have even observed that place-avoidance training causes synaptic plasticity of the MPP synaptic response in the suprapyramidal molecular layers of the DG with a corresponding change in DS_M but not DS_L, corroborating that the two pathways are distinctive and can be altered independently by experience (Chung et al., 2019).

The present findings point to a process of dynamic control of hippocampal information processing marked by transient physiological events across the trisynaptic pathway. During SG_{dom}, DG, CA3, and CA1 discharge is transiently elevated along with DG-CA3 cofiring (Figure 6), and there is SG frequency and phase synchronization between LPP inputs to DG and the *stratum radiatum* input from CA3 to CA1 (Figures 5 and 7), indicating involvement of the entire trisynaptic pathway, similar to SWRs (Buzsáki et al., 2003; Sullivan et al., 2011). During DS_M, SWR probability in a 20-ms window increases from 1.2% to 1.8% (Figure 3G), and place cell discharge is non-local during SWRs (Buzsáki, 2015; O'Neill et al., 2006; Papale et al., 2016; Sullivan et al., 2011) and during SG_{dom} (Figure 1; Dvorak et al., 2018).

The qualitative distinction between information signaled by lateral EC (LEC) and MEC is important in this context. The LEC transmits contextual information based on objects and egocentric information that constitutes the content of spatial experience (Knierim et al., 2013; Tsao et al., 2013; Wang et al., 2018), whereas the MEC transmits allocentric spatial signals such as direction, distance, borders, and speed (Hargreaves et al., 2005; Rowland et al., 2018; Sargolini et al., 2006; Ye et al., 2018). Remarkably, the MEC-originating DS_M signal that promotes SG_{dom} and switches CA1 to non-local positional memory processing is coincident with synchronization between CA3-transmitted SG inputs to CA1 and LEC-transmitted SG inputs to DG, rather than from MEC (Figures 5 and 7). Within the ''communication through coherence'' hypothesis (Fries et al., 2007), the LEC→DG and CA3→CA1 inputs have a privileged opportunity for information transfer via synchronized SG transmission, and so we speculate that perhaps while switching the hippocampal information processing mode, DS_M loads Ammon's horn with information from the LEC-delivered egocentric contents of experience. In this way, during DS_M, the consequent activation of CA3 may be preferentially influenced by contextual and egocentric, ecphoric retrieval cues delivered by the LEC inputs (Fernández-Ruiz et al., 2021; Kelemen and Fenton, 2013; Tulving et al., 1983). If these manifest as SG_{dom} because of the strong DS_M-associated activation of CA3 (Figures 6 and 7), then the result is control of CA1 output that overrides the default control that is exerted by the mid-frequency gamma-mediated

Author Manuscript Author Manuscript Author Manuscript Author Manuscript

ECIII input at *slm* (Brun et al., 2002). These *slm* inputs appear necessary for place cell firing (Brun et al., 2008). They also create permissive dendritic depolarization (Jarsky et al., 2005), but in principle, they can be shunted by the SG-associated inputs (Keeley et al., 2017) and are possibly actively inhibited as a consequence of DS_M (Figure 4F), all of which promote SG_{dom} (Figure 3H). As we have observed during SG_{dom}, CA1 discharge will signal non-local positions that, during a memory task, correspond to recollected places (Dvorak et al., 2018), and we observed here a correspondingly reduced local discharge by place cells in their firing fields (Figure 1), despite maintained CA1 firing (Figure 6C). The findings of a hippocampus-wide (Figures 6 and 7), DS_M-promoted SG_{dom} change to a non-local mode of information processing identifies a source of the overdispersion that is characteristic of place cells in CA1, CA3, and DG (Fenton et al., 2010; Fenton and Muller, 1998; Hok et al., 2012; Jackson and Redish, 2007; van Dijk and Fenton, 2018), and also grid cells, although we cannot conclude that the mechanism is the same (Nagele et al., 2020). The findings also offer an explanation for the possible utility of CA1's receiving two spatial inputs; the Schaffer collaterals provide place cell inputs that can be non-local and related to mental experience, whereas the temporoammonic pathway provides an input comprising components of place (grid cell distances, directional cells, border cells, and speed cells) more tethered to local, physical experience.

Limitations of the study

We set out to determine whether recollection-associated SG_{dom} in CA1 arises spontaneously within the hippocampus, perhaps like sharp waves (Chambers et al., 2021; Sullivan et al., 2011), or whether their occurrence in CA1 is controlled extrinsically (Figures 1E and 1F). The multiple lines of convergent evidence presented here indicate that DS_M, MEC-originating DS events promote CA1 SG_{dom} as a sequence of events, the earliest of which is a DS_M at the MEC termination zone in the DG that results ~7 ms later in facilitation of SG_{SR} input to CA1 and attenuation of MG_{SLM} input to CA1, both promoting SG_{dom}. Attempts to specifically cause or prevent DS_M events by manipulation of the MPP were unsuccessful (Figure S4). Accordingly, we do not provide direct causal evidence for the sequence of events, but the results also indicate that DS_Ms are not merely the result of synchronous MPP activation. DS_Ms are more likely the result of complex, robust, and redundant dynamics that may defy the causal inference that has become a popular goal (Jonas and Kording, 2017). Nonetheless, the findings definitively demonstrate external control of SG_{dom}; however, they cannot identify whether the controlling event is the DS_M or some other event that causes both the DS_M and control of the SG_{SR} and MG_{SLM} components that just happen to correspond to the transit time from DG to CA1 across the trisynaptic pathway (~7 ms). The present considerations are relevant to a recent report that the distinct MEC- and LEC-originating gamma oscillations selectively mediate allocentric spatial and object-centered hippocampal information processing, respectively (Fernández-Ruiz et al., 2021). In particular, their optogenetic manipulations targeting MG_{MPP} and SG_{LPP} likely also manipulated DS_M and DS_L, respectively. Electrical stimulation of the ventral hippocampus commissure activates excitation and inhibition in Ammon's horn, suppressing SWRs (Girardeau et al., 2009; Penttonen et al., 1997) and is sufficient to impair the consolidation of trace eyeblink conditioning specifically when the stimulation coincides with undifferentiated DSs. Not only is this consistent with DSs being part of a complex

Author Manuscript Author Manuscript Author Manuscript Author Manuscript

of memory-related network operations that extend across the trisynaptic pathway (Nokia et al., 2017), but in light of the present findings, it is possible that the reported effects on memory are the result of the manipulations on DS_M-mediated control of SG_{dom}, rather than the effects on gamma per se or SWRs.

STAR★METHODS

RESOURCE AVAILABILITY

Lead contact—Further information and requests for resources should be directed to the Lead Contact, André A. Fenton (afenton@nyu.edu).

Materials availability—This study did not generate new unique materials.

Data and code availability

- Electrophysiology and location data have been deposited at G-Node and are publicly available as of the date of publication. DOI is listed in the key resources table.
- All original code has been deposited at G-Node and is publicly available as of the date of publication. DOI is listed in the key resources table.
- Any additional information required to reanalyze the data reported in this paper is available from the lead contact upon request.

EXPERIMENTAL MODEL AND SUBJECT DETAILS

Subjects—These experiments were conducted under the NYU University Animal Welfare Committee (UAWC) Protocol IDs: 13–1427 and 12–1386. A total of 14 wild-type male mice with a mixed C57BL/6J background were used for the study. The mice were 3 – 6 months old during surgery. Nine mice were implanted with linear silicon arrays. Three mice were implanted with a metal head plate for head-fixed recording using linear silicon arrays and Neuropixels probes (Jun et al., 2017). Two mice from a previously published dataset were implanted with tetrodes (Dvorak et al., 2018).

METHOD DETAILS

Surgery—LFP recordings were collected using 32-channel (8 mice) and 16-channel (1 mouse) linear silicon array electrodes (Neuronexus, Ann Arbor, MI) with 50 μm spacing and 703 um^2 electrode area. The 32-channel electrodes spanned both CA1 and DG locations, and the 16-channel electrode spanned only DG locations. The electrodes were implanted stereotaxically under isoflurane anesthesia (2%, 1 L/min). The tip was aimed at −1.85 AP, ± 1.20 ML, −2.3 DV relative to bregma. The electrodes spanned the dorso-ventral axis of the dorsal hippocampus. Reference electrodes were aimed at the cerebellar white matter. The electrode assemblies were anchored to the skull using 3–4 bone screws with dental cement (Grip Cement, Dentsply, Milford DE). One anterior screw was used as a ground. A four-wire stimulating electrode bundle was made by twisting together four 75-μm diameter nichrome wires (California Fine Wire, Grover Beach, CA). The bundle was cut at an angle so as to span 0.5 mm. During surgery, the stimulating bundle was placed in the ipsilateral perforant

Author Manuscript Author Manuscript Author Manuscript Author Manuscript

path +0.5 AP, ± 4.1 ML, 1.0–1.6 DV from lambda. Evoked response waveforms were carefully checked with different pair combinations of stimulation electrode channels. In the mice that were used for head-fixed recordings, a titanium head plate was attached to the skull using dental cement and the exposed skull was covered with KwikSil, a low toxicity adhesive (World Precision Instruments, Sarasota, FL) and protected by attaching a plastic cup. All mice were allowed at least 1 week to recover. In mice that were used for head-fixed recordings, a secondary surgery was performed immediately before the experiment. The plastic cup and KwikSil were removed and a craniotomy was made at 1.85 AP, ± 1.20 ML relative to bregma to enable electrode placement. Between consecutive days of recordings, a KwikSil protective cup assembly was reattached to prevent infection.

Behavioral tasks—Nine mice with implanted linear silicon probe arrays and 2 mice implanted with tetrodes were trained in the active place avoidance task. Each day consisted of a 30 min rest session in the home-cage, which was placed in the recording chamber, followed by a 30-min place avoidance session. After habituation (shock off), a total of 3 training sessions (shock on) were administered to all animals, one session each day. A retention session with the shock on followed 1 week after. Electrophysiology data from 9 mice implanted with linear silicon probe arrays and recorded during rest were used for Figures 2, 3A–3G, and 5. Electrophysiology data from the same group recorded during place avoidance were used for Figures 1A, 1B, 3H, and 4. Electrophysiology data from the 2 mice implanted with tetrodes were used for Figures 1C and 1D. Two mice were recorded in a custom head-fixed setup using both Neuropixels and Neuronexus linear silicon probe arrays during 59 sessions (average length 15.7 ± 3.9 min) spread over multiple days. Mice were encouraged to walk using a custom water delivery system. Electrophysiology data recorded in head-fixed mice were used for Figures 6 and 7.

Electrophysiology recording—An amplifier board with 32 unipolar inputs and 3-axis accelerometer (RHD2132, Intan Technologies, Los Angeles, CA) was connected directly to the Neuronexus probe for signal amplification and digitization. A lightweight, counter-balanced cable (Intan Technologies, Los Angeles, CA) was used to power the amplifier board and the infrared LED used for tracking as well as to transmit digital data to the computer using a custom recording system connected to the USB port of a PC. The cable was connected through a lightweight commutator to enable free movement of the animal. The signal from each electrode was low-pass filtered (500 Hz) and digitized at 2 kHz. Evoked responses were obtained using a constant current stimulus isolation unit (WPI, Sarasota, FL; model: A365RC) that was used to deliver individual unipolar 100 μs stimulus pulses across the electrode pair. Evoked responses were low-pass filtered at 4 kHz and sampled at 8.12 kHz. In head-fixed recordings, the signal from a Neuropixels probe was filtered between 0.5 Hz and 1 kHz and sampled at 2.5 kHz for LFP recordings and filtered between 300 Hz and 10 kHz and sampled at 30 kHz for single unit recording. Both electrophysiology systems were synchronized using square TTL pulses generated by the Neuropixels system that was recorded by both systems. The animals were recorded during a 30-minute session in their home-cage during the first exposure to the experimental room. The mouse’s movements during recordings were monitored continuously using a

Author Manuscript Author Manuscript Author Manuscript Author Manuscript

video tracking system (Tracker, Bio-Signal Group, Acton, MA) that was synchronized to the electrophysiology data using the video frame pulses generated by the camera.

QUANTIFICATION AND STATISTICAL ANALYSIS

LFP and electrode localization—LFPs were localized by visual LFP inspection of sharp-wave ripples in CA1 *stratum pyramidale* and dentate spikes in the hilus of the dentate gyrus (Figure S1E). Electrode locations were verified histologically at the end of recordings (Figures S1F and S1G). In the mouse implanted with the 16-ch electrode array, only dentate LFPs were recorded because of the limited spatial span of the electrode.

Detection of SG_{dom} events—A published algorithm was used to extract oscillatory events from LFP or independent components obtained using ICA (Dvorak and Fenton, 2014). The LFP is transformed into a time-frequency power representation by convolving the LFP/IC signal with a group of complex Morlet wavelets and z-score normalizing each band-specific signal. Oscillatory events are detected as local peaks in the normalized 2-D time-frequency space. Detection of oscillation rates and SG_{dom} events was described previously (Dvorak et al., 2018). Oscillation rates (Figure 1A, lower) are computed as the number of detected events in a representative frequency range (30–50 for CA1 slow gamma, 70–90 Hz for CA1 mid-frequency gamma) in a 1 s window advanced by 0.25 s and smoothed using a 2.5 s moving average. SG/MG ratio (Figure 1A, lower) is computed as a ratio of CA1 slow gamma oscillation rate and CA1 mid-frequency gamma oscillation rate. SG_{dom} events, are defined as local peaks in the SG/MG ratio with prominence exceeding 1 and SG/MG ratio > 1 (corresponding to SG > MG).

Detection and classification of dentate spikes—The LFP channel with the largest visually identified amplitude of dentate spike was band-pass filtered 5–100 Hz and the amplitude was z-score normalized. Next, all local peaks in the band-pass signal were detected, and several features were extracted, including the amplitude difference between the DS maxima and the preceding as well as following minima, and also the spike width that was measured at the level of either the preceding or following minima, whichever was closer to the maxima. The spike amplitude distributions were further normalized by z-score normalization of the log-transformed amplitudes. Putative dentate spikes were selected if their prominence (difference between amplitude of the DS maxima and the smaller of either its preceding or the following minima) > 0.75 and when the width of the event was between 5 and 25 ms. The optimal values were selected based on analysis of the feature histograms.

Dentate spikes were classified as DS_L and DS_M based on their CSD profiles (Bragin et al., 1995). CSDs were calculated using the CSDplotter MATLAB toolbox (Pettersen et al., 2006) at the peak of a putative DS event. Independently for each recording, the CSD for each putative DS event was analyzed for local minima, corresponding to CSD sinks (Figure 2B). The histogram of detected local minima of all putative DS events was plotted and the local maxima that represented the highest probability of current sinks were manually identified (color dots in Figure 2B, middle). This analysis resulted in 4 locations corresponding to (from top to bottom) the outer and the middle molecular layers of the suprapyramidal DG blade, and the middle and the outer molecular layers of the

Author Manuscript Author Manuscript Author Manuscript Author Manuscript

infrapyramidal DG blade. DS_L and DS_M were then identified from the suprapyramidal DG blade as putative DS events with a sink occurring ± 25 μm around the location selected in the sink histogram (solid lines in Figure 2B, right). The average CSD profiles of classified DS events did not change when classification from infrapyramidal DG blade was used instead (dashed lines in Figure 2B, right). Putative DS events with sinks in both the outer and middle molecular layers (1.7 ± 1.5%; mean ± SD) as well as those with no sinks detected in either the outer or the middle molecular layers (30.5 ± 17.8%) were excluded from analyses. Only putative DS events with a sink exclusively in either the outer or the middle molecular layer (67.8 ± 18.3%) were classified as DS_L and DS_M respectively.

Detection of ripple events—We followed a previously published algorithm (Csicsvari et al., 1999) with several modifications to detect ripple events. We used the LFP recorded from the CA1 *stratum pyramidale* electrode, where ripples were identified visually. First, the signal was 150–300 Hz band-pass filtered. Next, we computed the sliding root-mean square (RMS) estimate in a 10-ms window. Next, we z-scored normalized the RMS estimate and detected the local maxima with $z > 3$. Finally, for each detected event, we computed the wavelet time-frequency representation of the LFP and for each detected event we extracted its frequency as a local peak in the time-frequency wavelet spectrum (similar to detection of gamma oscillations described earlier). Only events with frequencies between 130–250 Hz were selected for further analysis.

Independent components analysis of the LFP—We used independent component analysis (ICA) to extract the specific CA1 dendritic components (Fernández-Ruiz and Herreras, 2013; Fernández-Ruiz et al., 2017), which minimizes the impact of volume conducted signals and estimates the components that can be precisely matched to specific dendritic compartments. LFP signals that were recorded using linear silicon array electrodes were decomposed into individual dendritic components using a previously described procedure (Fernández-Ruiz and Herreras, 2013; Fernández-Ruiz et al., 2017; Makarov et al., 2010) with several modifications. First, LFP signals were filtered between 20 Hz and 150 Hz. Next, principal component analysis (PCA) was applied to the filtered LFP data in order to find out how many principal components explain over 99% of the signal variance in the data. Next, independent component analysis (ICA) was applied to the filtered LFP data using the FastICA MATLAB toolbox (Hyvärinen, 1999) by specifying the number of principal components that were obtained in the previous steps for both PCA-based dimensionality reduction and the target number of resulting independent components. Next, components of the unmixing matrix were used to compute CSDs of the individual voltage loadings for component localization and independent components (ICs) were processed using comodulogram analysis for frequency-based classification of components. Here, we took advantage of theta phase coupling of gamma oscillations, which can reveal a specific frequency footprint of each component (Schomburg et al., 2014). Specifically, the LFP from the *stratum pyramidale* electrode was filtered using a set of FIR filters with 2 Hz bandwidth, in the range 5–11 Hz followed by the Hilbert transform to obtain the phase of CA1 theta oscillations. Next, independent components were filtered using 20-Hz wide filters in the range 20–150 Hz followed by the Hilbert transform to obtain amplitude information from individual components. Details of the filters and filtering procedure were

Author Manuscript Author Manuscript Author Manuscript Author Manuscript

described previously (Dvorak and Fenton, 2014). The phase and amplitude information were then combined between all pairs of frequency bands used to obtain phase and amplitude information and a modulation index (Tort et al., 2010) was computed for each pair resulting in a comodulogram (Figures 3C and 5A) that reveals the peak coupling between the phase of theta and the amplitude of a given IC. We found that the ICA analysis provides better segregation of the independent components if the number of LFP channels is restricted before performing ICA. On the other hand, it is not possible to say which LFP channels to include in the analysis for best IC separation. Consequently, we performed a grid search, where we systematically repeated ICA for different numbers of included contiguous segments of LFP channels referenced either to *stratum pyramidale* for CA1 (Figure 3) or to the *hilus* for DG (Figure 5). The resulting CSD profiles of ICs were then visually compared and selected based on both the CSD profile of voltage loadings and a clearly isolated peak of coupling between theta phase and the amplitude of a given component. While this operation is extremely computationally intensive, it allowed robust detection of the corresponding components in all the mice we studied (Figure S2A).

Phase locking analysis—To study the phase coupling between different oscillatory rhythms, we used the phase locking value (PLV) estimate (Lachaux et al., 1999), which provides a good estimate of phase locking for signals where the volume conducted signals have been minimized by ICA (Vinck et al., 2011). To calculate PLV of a pair of signals, we used an array of complex Morlet wavelets spaced by 1 Hz between 20 Hz and 100 Hz convolved with each of the ICs in the pair to obtain the instantaneous phase of both ICs at a given frequency. Next, we computed the instantaneous phase difference between the two ICs, IC_1 and IC_2. Then, for all pairs of time offsets in the range −100 ms to +100 ms relative to the DS event and each frequency, we computed instantaneous phase differences across all DS events $\Delta\varphi(t,f) = \varphi_1(t,f) - \varphi_2(t,f)$. Finally, we computed PLV across DS events as $PLV = \frac{1}{N}\left|\sum_{n=1}^{N} exp(i \cdot \Delta\varphi(t,f))\right|$, where i is the imaginary unit, N is number of DS events, t is the offset relative to DS event and f is frequency used to filter the signal to obtain its phase. Repeating this algorithm for a range of frequencies and offsets relative to DS events generates a time-frequency PLV estimate that is centered at each type of DS (Figure 5C).

Detection of oscillatory cycles—To detect oscillatory cycles of oscillatory bursts (Figure 4), we started by correcting the polarity of ICs, because the polarity of an individual ICs is arbitrary (Hyvärinen, 1999). Here, we took advantage of the known relationship between hippocampal gamma oscillations < 100 Hz and the spectral leakage of spiking activity (Figure S2B), that can be observed > 150 Hz at *stratum pyramidale* (Dvorak and Fenton, 2014; Lasztóczi and Klausberger, 2016; Schomburg et al., 2012). We first created a set of Morlet wavelets covering 20–50 Hz for SG_{SR} or covering 60–90 Hz for MG_{SLM} and used them to obtain the instantaneous phase of the IC components at specific frequencies. Next, we filtered the LFP from *stratum pyramidale* in the frequency range 150–250 Hz followed by a Hilbert transform to obtain the amplitude of the high frequency activity that served as a proxy for spiking activity. Next, for each IC, we created a phase-amplitude histogram of 150–250 Hz amplitude distribution relative to the phase of the IC component either in the 20–50 Hz range or the 60–90 Hz range (Figure S2B). Finally, we visually compared the resulting relationships and corrected each component so that the 150–250 Hz

Author Manuscript Author Manuscript Author Manuscript Author Manuscript

spiking-proxy activity was maximal at the descending phase of the SG_{SR} close to the trough and the ascending phase of MG_{SLM} close to the trough (Figure S2B). This step allowed us to reliably correct the polarity of all components from all animals in order to reliably extract local minima of oscillatory bursts. After correcting the polarity of IC components, we detected oscillatory bursts as described earlier and then found local minima in the ± 50 ms window around an oscillatory peak for SG_{SR} and in the ± 29 ms window around the oscillatory peak for MG_{SLM} corresponding to 3 cycles of oscillatory activity centered at the oscillatory cycle with largest amplitude (Figure S2C). The timestamps of individual oscillatory cycles were recorded and used for later processing.

Single unit analysis—Single units were sorted using a published open-source algorithm Kilosort2 (Pachitariu et al., 2016) that is optimized for Neuropixels probes and takes advantage of GPU processing to improve algorithm performance. After automated clustering of the data, we selected only units with < 20% estimated contamination rate with spikes from other neurons that were computed from the refractory period violations relative to expected. We also excluded units with non-characteristic or noisy waveforms resulting in identifying a total of 9404 single units.

The units were then localized to neocortex, CA1, DG/CA3 and thalamus using three criteria: 1) the depth of the Neuropixels probe relative to the cortical surface, 2) localization of dentate spikes in the hilus of dentate gyrus and sharp wave ripples in CA1 *stratum pyramidale* and clustering of units along the depth of the linear Neuropixels array. The clustering of units into different regions becomes apparent when we plot the depth of the maximal amplitude of the average action potential waveform for each unit along the length of the probe (Figure S5A). The cluster of single units that overlaps with the detected location of sharp-wave ripples was classified as CA1, whereas the cluster of units that overlaps with the detected location of DS was classified as DG/CA3. The cluster of units between CA1 and the cortical surface was classified as neocortical neurons and the large amplitude units below DG/CA3 were classified as thalamic neurons. To separate CA3 from DG units, we used two additional criteria. First, we used the anatomical location, confirmed by histology, and considered CA3 units to only be from electrodes that were more lateral than +1.5 mm relative to the midline. Second, we took advantage of the asymmetric profile of the perforant path termination in DG that is apparent in the CSD profiles of LFPs that were recorded with Neuropixels probes and triggered by DS_M events (Figure 6B). ECII projections to the infrapyramidal molecular layers of DG terminate at the mediolateral extent at which CA3 begins, while ECII projections to the suprapyramidal molecular layers of DG continue in parallel with CA3 (Figures 6B and S1F). Electrodes that exhibited only a dorsal current sink were classified as CA3, while electrodes that exhibited a symmetrical pair of current sinks were classified as DG. To further classify DG cells as putative granule cells (GC) and mossy cells (MC) we took advantage of two identified locations, that of the granule cell layer at the CSD reversal between the current sink in the middle molecular layer and the current source in the hilus triggered by DS_M, and that of the maximal amplitude of the average action potential of a given cell. Cells within 150 μm of the CSD reversal were classified as GC, while cells deeper than 150 μm were classified as MC (Senzai and Buzsáki, 2017). This

Author Manuscript Author Manuscript Author Manuscript Author Manuscript

procedure resulted in localizing 1413 cells to neocortex, 6422 neurons to thalamus, 492 cells localized to CA1, 696 cells localized to DG and 285 cells localized to CA3.

To classify units into putative excitatory and inhibitory neurons we used a similar approach as in other studies (Jia et al., 2019; Senzai and Buzsáki, 2017; Talbot et al., 2018) and extracted several features associated with the average action potential waveshape and features associated with firing properties (Figure S5B). Datasets were split into DG cells and CA1 + CA3 cells because features of DG action potentials were visually different from those in CA1 + CA3 (Figure S5C). Consequently, the two datasets were independently analyzed using the k-Means algorithm implemented in JMP 14 software to identify three clusters corresponding to three types of neurons classified as principal cells (Es), narrow-waveform interneurons (INs) and wide-waveform interneurons (IWs). Classification of CA1+CA3 cells separately from DG cells led to the best classification results into the selected neuronal subtypes. In the analyses that follow, we only focus on E and In cells because of their maximal separation in the feature space (Figure 6A).

Peri-DS-event time cofiring histogram—We assessed the probability that a pair of cells would cofire relative to the occurrence of a dentate spike by computing a cofiring probability for each cell pair. The probability was computed in a 6 ms-long window centered on the dentate spike peak. The co-firing probability was compared to randomly sampled events to obtain a ratio of cofiring change. Statistical validation was computed using a t test between the cofiring probabilities during DS events and randomly sampled times. The significance threshold was corrected using Bonferroni's method.

Bayesian location decoding—To obtain estimates of the mouse's location based on single unit data, we used a published algorithm (Zhang et al., 1998), where the probability of the current location is defined as $P(\boldsymbol{x}|\boldsymbol{n}) = C(\tau,\boldsymbol{n})P(\boldsymbol{x})\left(\prod_{i=1}^{N} f_i(\boldsymbol{x})^{n_i}\right)\exp\left(-\tau\sum_{i=1}^{N} f_i(\boldsymbol{x})\right)$, where $C(\boldsymbol{\tau},\boldsymbol{n})$ is a normalization factor so that $\sum_x P(\boldsymbol{x}|\boldsymbol{n}) = 1$, $f_i(\boldsymbol{x})$ are firing rate maps for cells $i..N$ obtained either by binning the 2-D space into 32×32 bins (Figure 1C) or 1-D space (distance to shock zone) into 12 angular bins (Figure 1D), $P(\boldsymbol{x})$ is the dwell distribution, t is the length of the time window (500 ms), n_i is the number of spikes fired by the i-th cell in a given time window and $\boldsymbol{x}$ is the (x,y) position of the animal in the 2D analysis or the angular position in the 1D analysis. Only recordings with at least five high quality spatial or non-spatial putative pyramidal cells were analyzed. Time windows with no spikes were excluded from analysis. Decoded location probability during SG_{dom} (Figure 1D) was normalized by a decoded location probability during MG_{dom} (SG_{dom} functional counterpart), computed as local peaks in the ratio of CA1 mid-frequency gamma and CA1 slow gamma).

Statistical analyses were performed using JMP version 14 (SAS, Cary, NC) and MATLAB 2019b (Mathworks, Natick, MA). Significance was accepted at $p < 0.05$. Exact p values are reported throughout.

Supplementary Material

Refer to Web version on PubMed Central for supplementary material.

Author Manuscript Author Manuscript Author Manuscript Author Manuscript

ACKNOWLEDGMENTS

This work was supported by NIH grants R01NS105472 and R01MH099128.

REFERENCES

Ashhad S, and Feldman JL (2020). Emergent Elements of Inspiratory Rhythmogenesis: Network Synchronization and Synchrony Propagation. Neuron 106, 482–497.e4. [PubMed: 32130872]

Barth AM, Domonkos A, Fernandez-Ruiz A, Freund TF, and Varga V. (2018). Hippocampal Network Dynamics during Rearing Episodes. Cell Rep23, 1706–1715. [PubMed: 29742427]

Bragin A, Jandó G, Nádasdy Z, van Landeghem M, and Buzsáki G. (1995). Dentate EEG spikes and associated interneuronal population bursts in the hippocampal hilar region of the rat. J. Neurophysiol73, 1691–1705. [PubMed: 7643175]

Bramham CR (1998). Phasic boosting of medial perforant path-evoked granule cell output time-locked to spontaneous dentate EEG spikes in awake rats. J. Neurophysiol 79, 2825–2832. [PubMed: 9636089]

Brun VH, Otnass MK, Molden S, Steffenach HA, Witter MP, Moser MB, and Moser EI (2002). Place cells and place recognition maintained by direct entorhinal-hippocampal circuitry. Science 296, 2243–2246. [PubMed: 12077421]

Brun VH, Leutgeb S, Wu HQ, Schwarcz R, Witter MP, Moser EI, and Moser MB (2008). Impaired spatial representation in CA1 after lesion of direct input from entorhinal cortex. Neuron 57, 290–302. [PubMed: 18215625]

Buzsáki G. (2015). Hippocampal sharp wave-ripple: a cognitive biomarker for episodic memory and planning. Hippocampus25, 1073–1188. [PubMed: 26135716]

Buzsáki G, Buhl DL, Harris KD, Csicsvari J, Czéh B, and Morozov A. (2003). Hippocampal network patterns of activity in the mouse. Neuroscience116, 201–211. [PubMed: 12535953]

Chambers AR, Berge CN, and Vervaeke K. (2021). Cell-type-specific silence in thalamocortical circuits precedes hippocampal sharp-wave ripples. bioRxiv, 2021.2005.2005.442741.

Chung A, Garcia-Jou C, Dvorak D, Hussain N, and Fenton A. (2019). Learning to learn persistently modifies a cortical-hippocampal excitatory-inhibitory subcircuit. bioRxiv10.1101/817627.

Colgin LL (2015). Do slow and fast gamma rhythms correspond to distinct functional states in the hippocampal network? Brain Res 1621, 309–315. [PubMed: 25591484]

Csicsvari J, Hirase H, Czurkó A, Mamiya A, and Buzsáki G. (1999). Fast network oscillations in the hippocampal CA1 region of the behaving rat. J. Neurosci19, RC20. [PubMed: 10436076]

de Almeida L, Idiart M, and Lisman JE (2009). A second function of gamma frequency oscillations: an E%-max winner-take-all mechanism selects which cells fire. J. Neurosci 29, 7497–7503. [PubMed: 19515917]

Dvorak D, and Fenton AA (2014). Toward a proper estimation of phase-amplitude coupling in neural oscillations. J. Neurosci. Methods 225, 42–56. [PubMed: 24447842]

Dvorak D, Radwan B, Sparks FT, Talbot ZN, and Fenton AA (2018). Control of recollection by slow gamma dominating mid-frequency gamma in hippocampus CA1. PLoS Biol 16, e2003354. [PubMed: 29346381]

English DF, McKenzie S, Evans T, Kim K, Yoon E, and Buzsáki G. (2017). Pyramidal Cell-Interneuron Circuit Architecture and Dynamics in Hippocampal Networks. Neuron96, 505–520.e7. [PubMed: 29024669]

Fenton AA, and Muller RU (1998). Place cell discharge is extremely variable during individual passes of the rat through the firing field. Proc. Natl. Acad. Sci. USA 95, 3182–3187. [PubMed: 9501237]

Fenton AA, Lytton WW, Barry JM, Lenck-Santini PP, Zinyuk LE, Kubík S, Bures J, Poucet B, Muller RU, and Olypher AV (2010). Attention-like modulation of hippocampus place cell discharge. J. Neurosci 30, 4613–4625. [PubMed: 20357112]

Fernández-Ruiz A, and Herreras O. (2013). Identifying the synaptic origin of ongoing neuronal oscillations through spatial discrimination of electric fields. Front. Comput. Neurosci7, 5. [PubMed: 23408586]

Author Manuscript Author Manuscript Author Manuscript Author Manuscript

Fernández-Ruiz A, Muñoz S, Sancho M, Makarova J, Makarov VA, and Herreras O. (2013). Cytoarchitectonic and dynamic origins of giant positive local field potentials in the dentate gyrus. J. Neurosci33, 15518–15532. [PubMed: 24068819]

Fernández-Ruiz A, Oliva A, Nagy GA, Maurer AP, Berényi A, and Buzsáki G. (2017). Entorhinal-CA3 Dual-Input Control of Spike Timing in the Hippocampus by Theta-Gamma Coupling. Neuron93, 1213–1226.e5. [PubMed: 28279355]

Fernández-Ruiz A, Oliva A, Soula M, Rocha-Almeida F, Nagy GA, Martin-Vazquez G, and Buzsáki G. (2021). Gamma rhythm communication between entorhinal cortex and dentate gyrus neuronal assemblies. Science372, eabf3119. [PubMed: 33795429]

Fries P, Nikolić D, and Singer W. (2007). The gamma cycle. Trends Neurosci30, 309–316. [PubMed: 17555828]

Garner AR, Rowland DC, Hwang SY, Baumgaertel K, Roth BL, Kentros C, and Mayford M. (2012). Generation of a synthetic memory trace. Science335, 1513–1516. [PubMed: 22442487]

Girardeau G, Benchenane K, Wiener SI, Buzsáki G, and Zugaro MB (2009). Selective suppression of hippocampal ripples impairs spatial memory. Nat. Neurosci 12, 1222–1223. [PubMed: 19749750]

Hargreaves EL, Rao G, Lee I, and Knierim JJ (2005). Major dissociation between medial and lateral entorhinal input to dorsal hippocampus. Science 308, 1792–1794. [PubMed: 15961670]

Harris KD, Csicsvari J, Hirase H, Dragoi G, and Buzsáki G. (2003). Organization of cell assemblies in the hippocampus. Nature424, 552–556. [PubMed: 12891358]

Headley DB, Kanta V, and Paré D. (2017). Intra- and interregional cortical interactions related to sharp-wave ripples and dentate spikes. J. Neurophysiol117, 556–565. [PubMed: 27832604]

Hebb DO (1949). The Organization of Behavior: A Neuropsychological Theory (John Wiley & Sons).

Hok V, Chah E, Reilly RB, and O'Mara SM (2012). Hippocampal dynamics predict interindividual cognitive differences in rats. J. Neurosci 32, 3540–3551. [PubMed: 22399776]

Hyvärinen A. (1999). Fast and robust fixed-point algorithms for independent component analysis. IEEE Trans. Neural Netw10, 626–634. [PubMed: 18252563]

Jackson J, and Redish AD (2007). Network dynamics of hippocampal cell-assemblies resemble multiple spatial maps within single tasks. Hippocampus 17, 1209–1229. [PubMed: 17764083]

Jarsky T, Roxin A, Kath WL, and Spruston N. (2005). Conditional dendritic spike propagation following distal synaptic activation of hippocampal CA1 pyramidal neurons. Nat. Neurosci8, 1667–1676. [PubMed: 16299501]

Jia X, Siegle JH, Bennett C, Gale SD, Denman DJ, Koch C, and Olsen SR (2019). High-density extracellular probes reveal dendritic backpropagation and facilitate neuron classification. J. Neurophysiol 121, 1831–1847. [PubMed: 30840526]

Johnson A, and Redish AD (2007). Neural ensembles in CA3 transiently encode paths forward of the animal at a decision point. J. Neurosci 27, 12176–12189. [PubMed: 17989284]

Jonas E, and Kording KP (2017). Could a Neuroscientist Understand a Microprocessor? PLoS Comput. Biol 13, e1005268. [PubMed: 28081141]

Jun JJ, Steinmetz NA, Siegle JH, Denman DJ, Bauza M, Barbarits B, Lee AK, Anastassiou CA, Andrei A, Aydın Ç., et al. (2017). Fully integrated silicon probes for high-density recording of neural activity. Nature 551, 232–236. [PubMed: 29120427]

Kanter BR, Lykken CM, Avesar D, Weible A, Dickinson J, Dunn B, Borgesius NZ, Roudi Y, and Kentros CG (2017). A Novel Mechanism for the Grid-to-Place Cell Transformation Revealed by Transgenic Depolarization of Medial Entorhinal Cortex Layer II. Neuron 93, 1480–1492.e6. [PubMed: 28334610]

Kay K, Chung JE, Sosa M, Schor JS, Karlsson MP, Larkin MC, Liu DF, and Frank LM (2020). Constant Sub-second Cycling between Representations of Possible Futures in the Hippocampus. Cell 180, 552–567.e25. [PubMed: 32004462]

Keeley S, Fenton AA, and Rinzel J. (2017). Modeling fast and slow gamma oscillations with interneurons of different subtype. J. Neurophysiol117, 950–965. [PubMed: 27927782]

Kelemen E, and Fenton AA (2010). Dynamic grouping of hippocampal neural activity during cognitive control of two spatial frames. PLoS Biol 8, e1000403. [PubMed: 20585373]

Author Manuscript Author Manuscript Author Manuscript Author Manuscript

Kelemen E, and Fenton AA (2013). Key features of human episodic recollection in the cross-episode retrieval of rat hippocampus representations of space. PLoS Biol 11, e1001607. [PubMed: 23874154]

Kelemen E, and Fenton AA (2016). Coordinating different representations in the hippocampus. Neurobiol. Learn. Mem 129, 50–59. [PubMed: 26748023]

Knierim JJ, Neunuebel JP, and Deshmukh SS (2013). Functional correlates of the lateral and medial entorhinal cortex: objects, path integration and local-global reference frames. Philos. Trans. R. Soc. Lond. B Biol. Sci 369, 20130369. [PubMed: 24366146]

Lachaux JP, Rodriguez E, Martinerie J, and Varela FJ (1999). Measuring phase synchrony in brain signals. Hum. Brain Mapp 8, 194–208. [PubMed: 10619414]

Lasztóczi B, and Klausberger T. (2014). Layer-specific GABAergic control of distinct gamma oscillations in the CA1 hippocampus. Neuron81, 1126–1139. [PubMed: 24607232]

Lasztóczi B, and Klausberger T. (2016). Hippocampal Place Cells Couple to Three Different Gamma Oscillations during Place Field Traversal. Neuron91, 34–40. [PubMed: 27387648]

Makarov VA, Makarova J, and Herreras O. (2010). Disentanglement of local field potential sources by independent component analysis. J. Comput. Neurosci29, 445–457. [PubMed: 20094907]

McNaughton BL (1980). Evidence for two physiologically distinct perforant pathways to the fascia dentata. Brain Res 199, 1–19. [PubMed: 7407615]

Miao C, Cao Q, Ito HT, Yamahachi H, Witter MP, Moser MB, and Moser EI (2015). Hippocampal Remapping after Partial Inactivation of the Medial Entorhinal Cortex. Neuron 88, 590–603. [PubMed: 26539894]

Mizuseki K, Royer S, Diba K, and Buzsáki G. (2012). Activity dynamics and behavioral correlates of CA3 and CA1 hippocampal pyramidal neurons. Hippocampus22, 1659–1680. [PubMed: 22367959]

Nagele J, Herz AVM, and Stemmler MB (2020). Untethered firing fields and intermittent silences: why grid-cell discharge is so variable. Hippocampus 30, 367–383. [PubMed: 32045073]

Nokia MS, Gureviciene I, Waselius T, Tanila H, and Penttonen M. (2017). Hippocampal electrical stimulation disrupts associative learning when targeted at dentate spikes. J. Physiol595, 4961–4971. [PubMed: 28426128]

O'Neill J, Senior T, and Csicsvari J. (2006). Place-selective firing of CA1 pyramidal cells during sharp wave/ripple network patterns in exploratory behavior. Neuron49, 143–155. [PubMed: 16387646]

Olypher AV, Lánský P, and Fenton AA (2002a). On the location-specific positional and extra-positional information in the discharge of rat hippocampal cells. Biosystems 67, 167–175. [PubMed: 12459296]

Olypher AV, Lánský P, and Fenton AA (2002b). Properties of the extra-positional signal in hippocampal place cell discharge derived from the overdispersion in location-specific firing. Neuroscience 111, 553–566. [PubMed: 12031343]

Pachitariu M, Steinmetz N, Kadir S, Carandini M, and Harris KD (2016). Kilosort: realtime spike-sorting for extracellular electrophysiology with hundreds of channels. bioRxiv 10.1101/061481.

Papale AE, Zielinski MC, Frank LM, Jadhav SP, and Redish AD (2016). Interplay between Hippocampal Sharp-Wave-Ripple Events and Vicarious Trial and Error Behaviors in Decision Making. Neuron 92, 975–982. [PubMed: 27866796]

Pastalkova E, Itskov V, Amarasingham A, and Buzsáki G. (2008). Internally generated cell assembly sequences in the rat hippocampus. Science321, 1322–1327. [PubMed: 18772431]

Penttonen M, Kamondi A, Sik A, Acsády L, and Buzsáki G. (1997). Feed-forward and feed-back activation of the dentate gyrus in vivo during dentate spikes and sharp wave bursts. Hippocampus7, 437–450. [PubMed: 9287083]

Pettersen KH, Devor A, Ulbert I, Dale AM, and Einevoll GT (2006). Current-source density estimation based on inversion of electrostatic forward solution: effects of finite extent of neuronal activity and conductivity discontinuities. J. Neurosci. Methods 154, 116–133. [PubMed: 16436298]

Renart A, de la Rocha J, Bartho P, Hollender L, Parga N, Reyes A, and Harris KD (2010). The asynchronous state in cortical circuits. Science 327, 587–590. [PubMed: 20110507]

Rolls ET, and Treves A. (1998). Neural Networks and Brain Function (Oxford University Press).

Author Manuscript Author Manuscript Author Manuscript Author Manuscript

Rowland DC, Obenhaus HA, Skytøen ER, Zhang Q, Kentros CG, Moser EI, and Moser MB (2018). Functional properties of stellate cells in medial entorhinal cortex layer II. eLife 7, e36664. [PubMed: 30215597]

Sargolini F, Fyhn M, Hafting T, McNaughton BL, Witter MP, Moser MB, and Moser EI (2006). Conjunctive representation of position, direction, and velocity in entorhinal cortex. Science 312, 758–762. [PubMed: 16675704]

Schlesiger MI, Boublil BL, Hales JB, Leutgeb JK, and Leutgeb S. (2018). Hippocampal Global Remapping Can Occur without Input from the Medial Entorhinal Cortex. Cell Rep22, 3152–3159. [PubMed: 29562172]

Schomburg EW, Anastassiou CA, Buzsáki G, and Koch C. (2012). The spiking component of oscillatory extracellular potentials in the rat hippocampus. J. Neurosci32, 11798–11811. [PubMed: 22915121]

Schomburg EW, Fernández-Ruiz A, Mizuseki K, Berényi A, Anastassiou CA, Koch C, and Buzsáki G. (2014). Theta phase segregation of input-specific gamma patterns in entorhinal-hippocampal networks. Neuron84, 470–485. [PubMed: 25263753]

Senzai Y, and Buzsáki G. (2017). Physiological Properties and Behavioral Correlates of Hippocampal Granule Cells and Mossy Cells. Neuron93, 691–704.e5. [PubMed: 28132824]

Stark E, and Abeles M. (2009). Unbiased estimation of precise temporal correlations between spike trains. J. Neurosci. Methods179, 90–100. [PubMed: 19167428]

Sullivan D, Csicsvari J, Mizuseki K, Montgomery S, Diba K, and Buzsáki G. (2011). Relationships between hippocampal sharp waves, ripples, and fast gamma oscillation: influence of dentate and entorhinal cortical activity. J. Neurosci31, 8605–8616. [PubMed: 21653864]

Talbot ZN, Sparks FT, Dvorak D, Curran BM, Alarcon JM, and Fenton AA (2018). Normal CA1 Place Fields but Discoordinated Network Discharge in a Fmr1-Null Mouse Model of Fragile X Syndrome. Neuron 97, 684–697.e4. [PubMed: 29358017]

Tort AB, Komorowski R, Eichenbaum H, and Kopell N. (2010). Measuring phase-amplitude coupling between neuronal oscillations of different frequencies. J. Neurophysiol104, 1195–1210. [PubMed: 20463205]

Traub RD, Whittington MA, Gutiérrez R, and Draguhn A. (2018). Electrical coupling between hippocampal neurons: contrasting roles of principal cell gap junctions and interneuron gap junctions. Cell Tissue Res373, 671–691. [PubMed: 30112572]

Tsao A, Moser MB, and Moser EI (2013). Traces of experience in the lateral entorhinal cortex. Curr. Biol 23, 399–405. [PubMed: 23434282]

Tulving E, Le Voi ME, Routh DA, and Loftus E. (1983). Ecphoric processes in episodic memory. Philos. Trans. R. Soc. Lond. B Biol. Sci302, 361–371.

van Dijk MT, and Fenton AA (2018). On How the Dentate Gyrus Contributes to Memory Discrimination. Neuron 98, 832–845.e5. [PubMed: 29731252]

Vinck M, Oostenveld R, van Wingerden M, Battaglia F, and Pennartz CM (2011). An improved index of phase-synchronization for electrophysiological data in the presence of volume-conduction, noise and sample-size bias. Neuroimage 55, 1548–1565. [PubMed: 21276857]

Wang C, Chen X, Lee H, Deshmukh SS, Yoganarasimha D, Savelli F, and Knierim JJ (2018). Egocentric coding of external items in the lateral entorhinal cortex. Science 362, 945–949. [PubMed: 30467169]

Whittington MA, Traub RD, and Jefferys JG (1995). Synchronized oscillations in interneuron networks driven by metabotropic glutamate receptor activation. Nature 373, 612–615. [PubMed: 7854418]

Wu CT, Haggerty D, Kemere C, and Ji D. (2017). Hippocampal awake replay in fear memory retrieval. Nat. Neurosci20, 571–580. [PubMed: 28218916]

Ye J, Witter MP, Moser MB, and Moser EI (2018). Entorhinal fast-spiking speed cells project to the hippocampus. Proc. Natl. Acad. Sci. USA 115, E1627–E1636. [PubMed: 29386397]

Zhang K, Ginzburg I, McNaughton BL, and Sejnowski TJ (1998). Interpreting neuronal population activity by reconstruction: unified framework with application to hippocampal place cells. J. Neurophysiol 79, 1017–1044. [PubMed: 9463459]

Author Manuscript Author Manuscript Author Manuscript Author Manuscript

Highlights

- CA1 represents distant, recollected locations during slow gamma dominance (SG_{dom})
- Medial entorhinal cortex-originating dentate spikes (DS_M) promote non-local firing
- DS_M promotes coordinated E-I coupled discharge in DG, CA3, and CA1 leading to SG_{dom}
- DG and CA1 sync during DS_M, optimizing spike-field timing for information transfer

Author Manuscript Author Manuscript Author Manuscript Author Manuscript

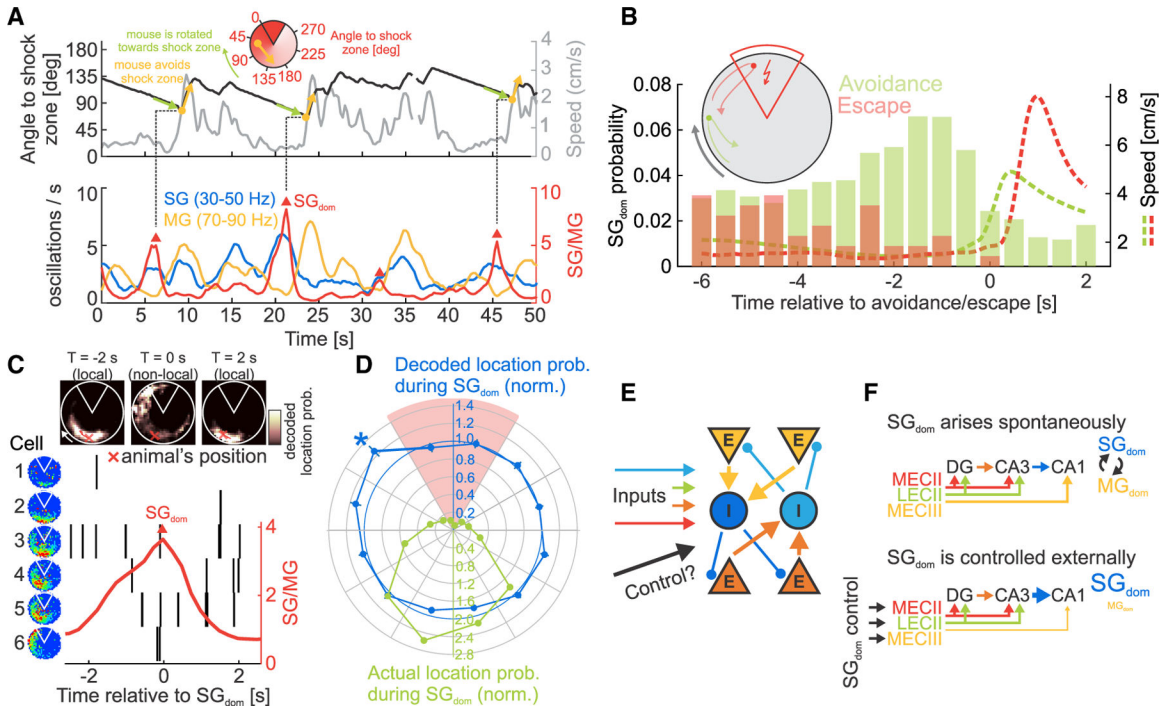

Figure 1. SG_{dom} is a biomarker of memory recollection

(A) Avoidances (yellow vectors) mark evasive movements with preceding stillness (green vectors) away from the shock zone without receiving shock. SG_{dom} detected as local maxima (red triangles) in the ratio (red line) of rates of CA1 slow (blue; 30–50 Hz) and mid-frequency (yellow; 70–90 Hz) gamma oscillations, precede avoidance movements by 1–2 s.

(B) SG_{dom} probability histogram before avoidance (green; success = no shock) and escape (red; failure = shocked).

(C) CA1 single-unit discharge (vertical black lines) of a 6-cell ensemble around a SG_{dom} event (red triangle). The firing rate map of each cell is shown on the left. The 2D posterior probability distributions computed using Bayesian decoding are shown at the top overlaid with the 5-s track of the mouse (red line) and current location (red cross). During SG_{dom}, the otherwise accurate Bayesian posterior decodes to the shock zone, away from the mouse's current location.

(D) Normalized circular probability distributions of mouse locations (green) and decoded locations (blue) during SG_{dom} (normalization using non-SG_{dom} events). *Significant deviation from 1 (t_{778} = 3.10, p = 0.002, Bonferroni's correction). While SG_{dom} happens predominantly when the mouse is opposite the shock zone (green), discharge during SG_{dom} decodes to locations of shock zone entries (blue).

(E) Schematic network with winner-take-all dynamics, composed of excitatory (E) and inhibitory (I) neurons, excitatory inputs, and a possible external control signal.

(F) Two hypotheses for hippocampal information-processing control (upper) intrinsic, intrahippocampal and (lower) extrinsic, extrahippocampal control.

Data in (B) and (D) from 2 mice.

Author Manuscript Author Manuscript Author Manuscript Author Manuscript

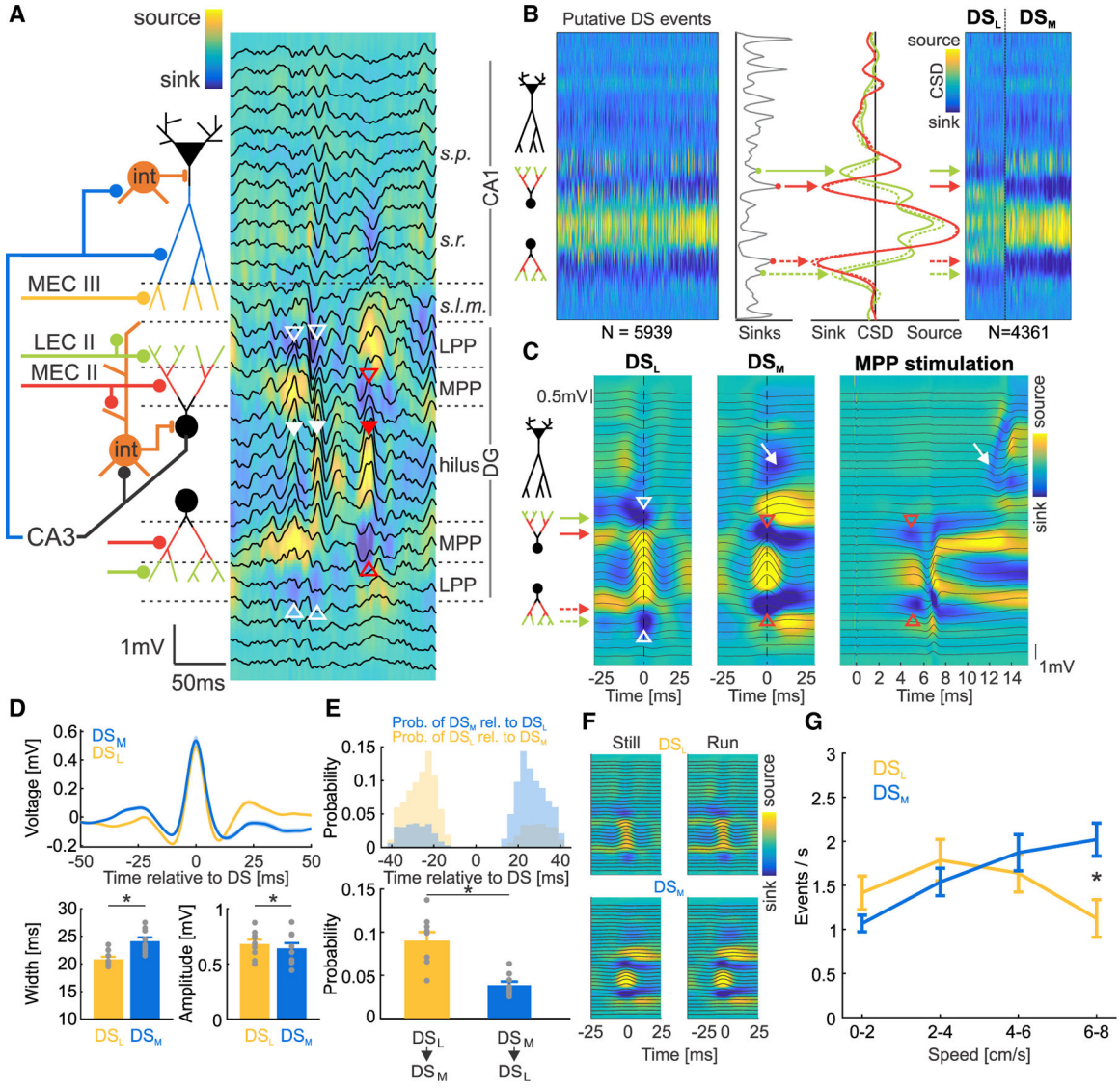

Figure 2. Current source density (CSD) analysis classifies 2 types of dentate spikes (DSs) with distinct anatomical, temporal, and behavioral properties

(A) DS_L (full white arrowheads) is identified by a pair of CSD sinks in the outer molecular layers of DG (empty white arrowheads) at the LECII projection termination. DS_M (full red arrowheads) is identified by a pair of CSD sinks in the middle molecular layers of DG (empty red arrowheads) at the MECII projection termination. Background color represents CSD. Black traces represent the LFP. Schematic (left) illustrating hypothesized components of DS generation and mechanism of CA1 SG_{dom} control.

(B) CSD of putative DS events (left) and histogram of local minima in CSD profiles (center) shows peaks aligned with pairs of sink bands in the outer (solid green and dashed green traces) and middle (solid red and dashed red traces) molecular layers. CSD profiles (right) of the 2 types of DS events.

(C) Average CSDs of DS_L (left) and DS_M (center), with DS_L sinks at outer molecular layers (white empty arrowheads) and DS_M sinks at middle molecular layers (red empty arrowheads). The CSD of the evoked response to medial perforant path (MPP) stimulation

Author Manuscript Author Manuscript Author Manuscript Author Manuscript

(right) evokes sinks (red empty arrowheads) at the same locations of the DS_M sinks. A ~6-ms latency sink at CA1 *stratum radiatum* occurs after both the MPP-evoked response and DS_M (white arrow), but not after DS_L.

(D) Average LFP of DS_L (yellow) and DS_M (blue), with their width and amplitude comparisons (bottom).

(E) Histograms illustrate that DS_M often follows DS_L (top) and the probability of observing $DS_L \rightarrow DS_M$ versus $DS_M \rightarrow DS_L$ pairs (bottom).

(F) Average CSDs of DS_L (top) and DS_M (bottom) during stillness (speed <2 cm/s; left) and running (speed >3 cm/s; right).

(G) Relationship between DS rates and running speed.

Averages ± SEM are plotted.

Author Manuscript Author Manuscript Author Manuscript Author Manuscript

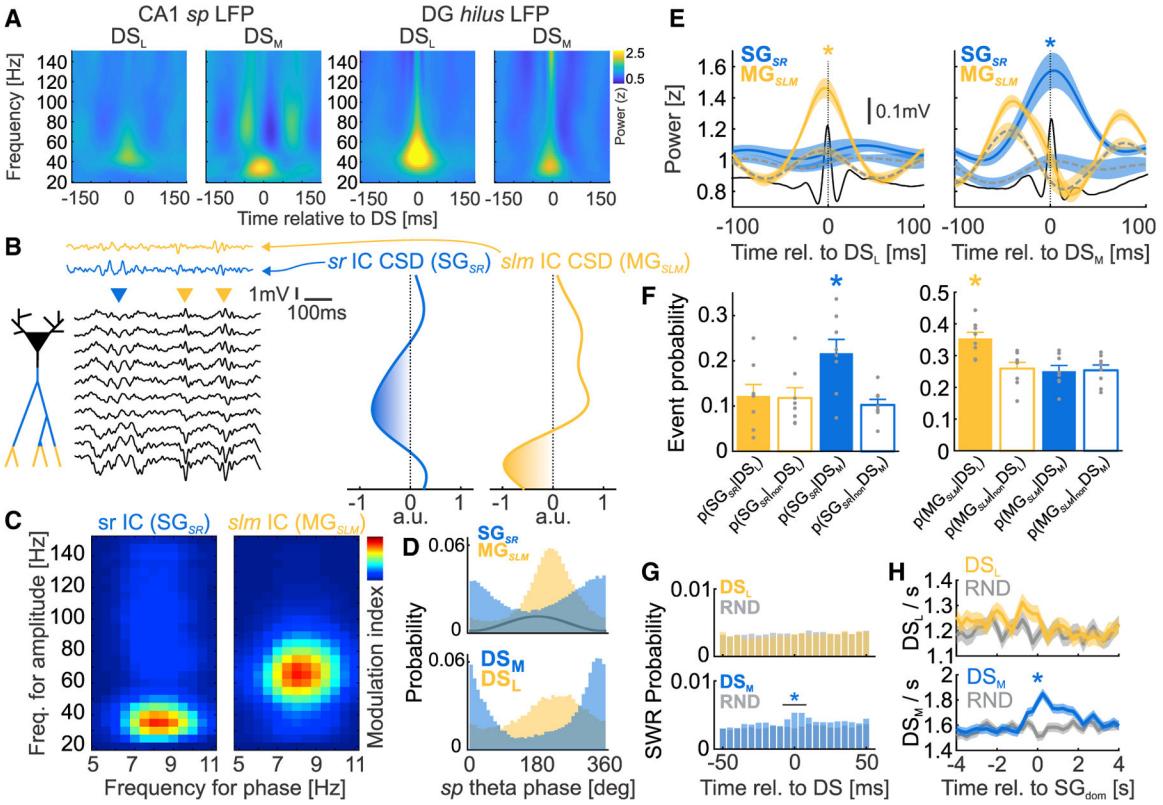

Figure 3. DSs modulate SG_{dom} and gamma oscillatory activity in CA1

(A) Average wavelet spectrogram of CA1 *stratum pyramidale* LFP (left) and DG hilar LFP (right), triggered by DS_L and DS_M events reveal volume-conducted DS spectral leakage in the 30–50 Hz range, with higher peak frequency associated with narrower DS_L events and lower peak frequency associated with wider DS_M events, as expected (compare with Figure 2D).

(B) ICA decomposition of CA1 LFPs identifies 2 ICs <100 Hz that correspond to *stratum radiatum* dendritic input (SG_{SR}, CA1 SG, blue), and *stratum lacunosum moleculare* dendritic input (MG_{SLM}, CA1 mid-frequency gamma, yellow). Arrowheads mark SG_{SR} (blue) and MG_{SLM} (yellow) oscillatory events in the LFP. The CSDs of ICA voltage loadings (right) show a SG_{SR} sink in *stratum radiatum* and a MG_{SLM} sink in *stratum lacunosum moleculare*.

(C) Comodulograms between the phase of CA1 *stratum pyramidale* theta (5–11 Hz) and the SG_{SR} and MG_{SLM} gamma amplitudes in the 20- to 150-Hz frequency range show slow gamma peaks for SG_{SR} and mid-frequency gamma peaks for MG_{SLM}.

(D) Theta phase (black line) distribution of SG_{SR} (blue) and MG_{SLM} (yellow) oscillatory events (top) compared to theta phase distribution of DS_M (blue) and DS_L (yellow) events (bottom).

(E) Power averages of SG_{SR} (blue) and MG_{SLM} (yellow) centered on DS_L (left) and DS_M (right). T = 0 marks the DS peak. Gray dashed lines show IC power profiles at random times sampled from the same theta phase distributions as the corresponding DS_L and DS_M events. Black lines are DS_L and DS_M event averages.

Author Manuscript Author Manuscript Author Manuscript Author Manuscript

(F) Coincidence of the DS and IC oscillatory events detected from SG_{SR} (left) and MG_{SLM} (right) at random times.
(G) SWR probability distribution relative to DS_L (top), DS_M (bottom), and random times (gray) during stillness.
(H) Rates of DS_L (top) and DS_M (bottom) centered at SG_{dom} (color) and randomly selected times (gray).
Averages ± SEM are plotted.

Author Manuscript Author Manuscript Author Manuscript Author Manuscript

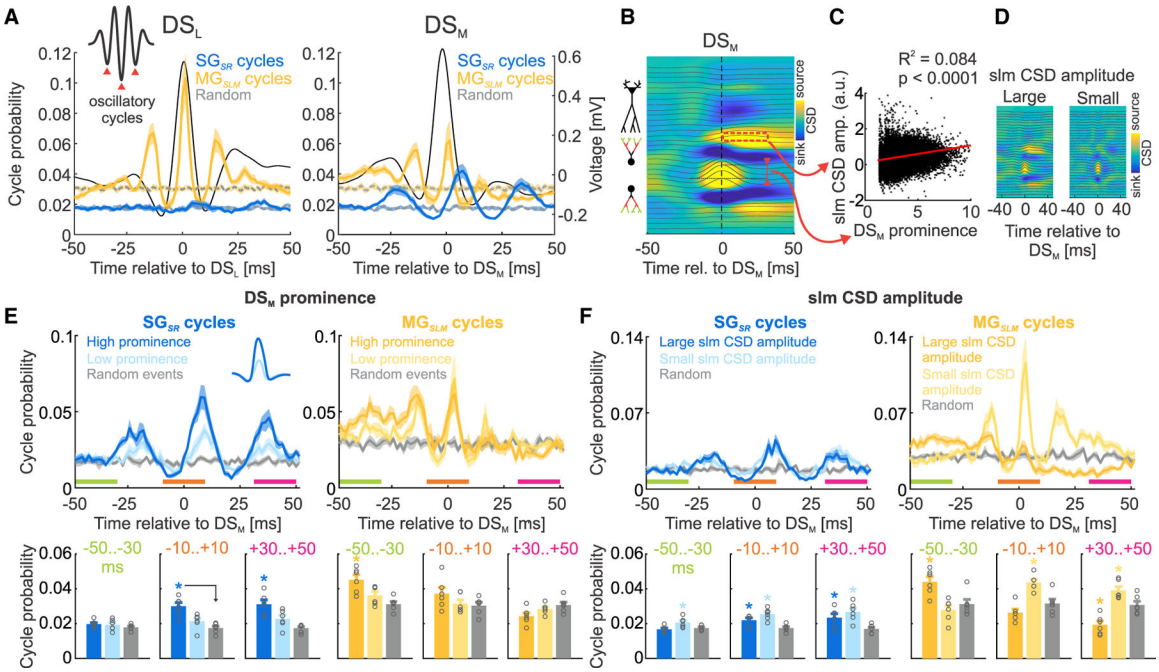

Figure 4. DS_M controls the oscillatory components of SG dominance

(A) Probability of oscillatory cycles (inset, red arrowheads) detected in SG_{SR} (blue) and MG_{SLM} (yellow) relative to DS_L (left), DS_M (right), and random events (gray). Average DS waveforms are black.

(B) CSD indicating DS_M prominence (red line with reversed arrows) and amplitude of the *slm* CSD source that follows DS_M (red rectangle).

(C) Scatterplot of DS_M prominence versus the *slm* CSD source during DS_M, with linear fit (red).

(D) Average DS_M CSD of the 10% largest (left) and smallest (right) *slm* CSD sources; the DS_M prominence is similar.

(E and F) Probability of SG_{SR} cycles (blue; left) and MG_{SLM} cycles (yellow; right) during the 10% largest (dark color), and smallest (light color) DS_M (E) prominence, and (F) *slm* CSD source amplitude; random events (gray) and comparisons BEFORE (−50 to −30 ms), DURING (−10 to +10 ms), and AFTER (30 to 50 ms) the DS_M events.

Averages ± SEM are plotted.

Author Manuscript Author Manuscript Author Manuscript Author Manuscript

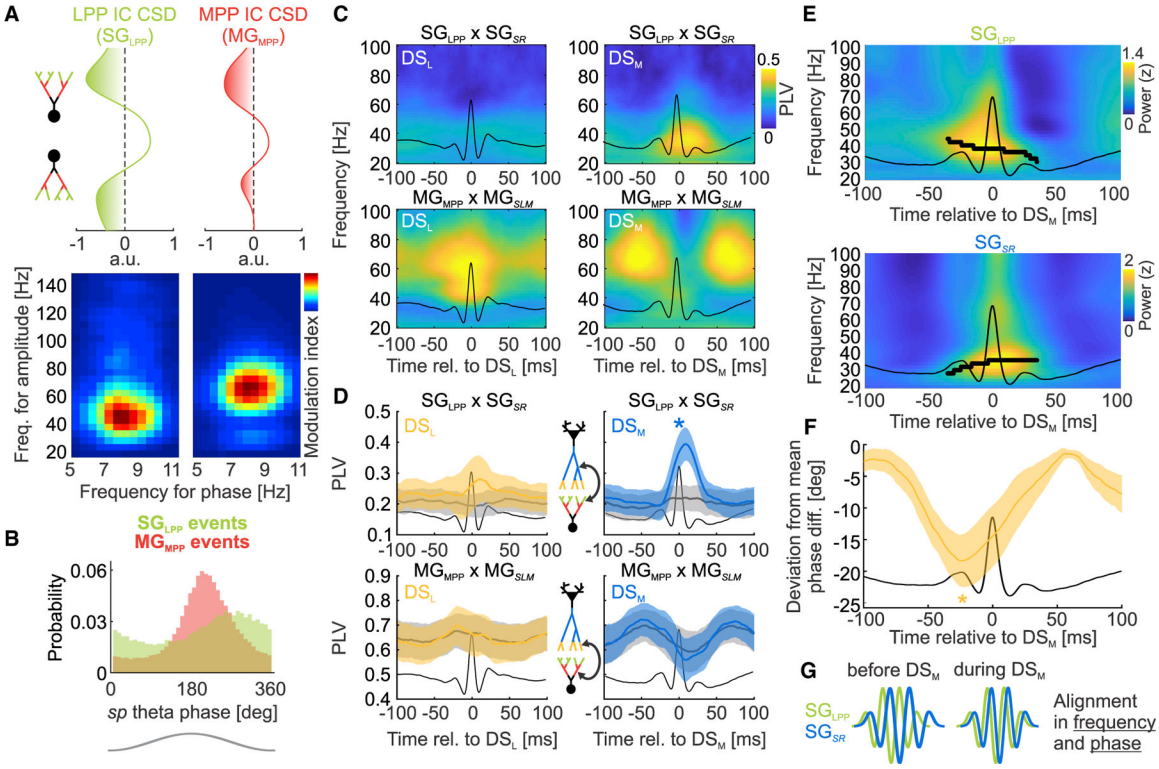

Figure 5. DS_M synchronizes the SG oscillatory inputs from LPP to DG and from CA3 to CA1 *stratum radiatum*

(A) CSDs of ICA voltage loadings (top) of the LPP IC (SG_{LPP}; green) and the MPP IC (MG_{MPP}; red) in the DG. Comodulograms (bottom) between the phase of CA1 theta (5–11 Hz) and the amplitude of both IC components across 20–150 Hz.

(B) Theta phase distribution of SG_{LPP} (green) and MG_{MPP} (red) oscillatory events.

(C) Example of phase locking value (PLV) between DG and CA1 SGs ($SG_{LPP} \times SG_{SR}$; top) and between DG and CA1 mid-frequency gammas ($MG_{MPP} \times MG_{SLM}$; bottom) time locked to DS_L (left) and DS_M (right).

(D) Group PLV measures averaged across SG (25–45 Hz for SG_{LPP} and SG_{SR}) and mid-frequency gamma (45–85 Hz for MG_{LPP} and MG_{SLM}). Gray: PLV profiles of random samples from the corresponding DS_L and DS_M theta phase distributions.

(E) Average wavelet spectrogram of SG_{LPP} (top) and SG_{SR} (bottom) around the time of DS_M (T = 0 ms). Black dots indicate frequency of peak power at each time point ± 40 ms.

(F) Group average of how much the instantaneous phase differences between SG_{LPP} and SG_{SR} differ from the mean phase difference. Averages ± SEM and average DS waveforms (black) are plotted.

(G) Schematic of frequency and phase alignment of SG_{LPP} and SG_{SR} during DS_M.

Author Manuscript Author Manuscript Author Manuscript Author Manuscript

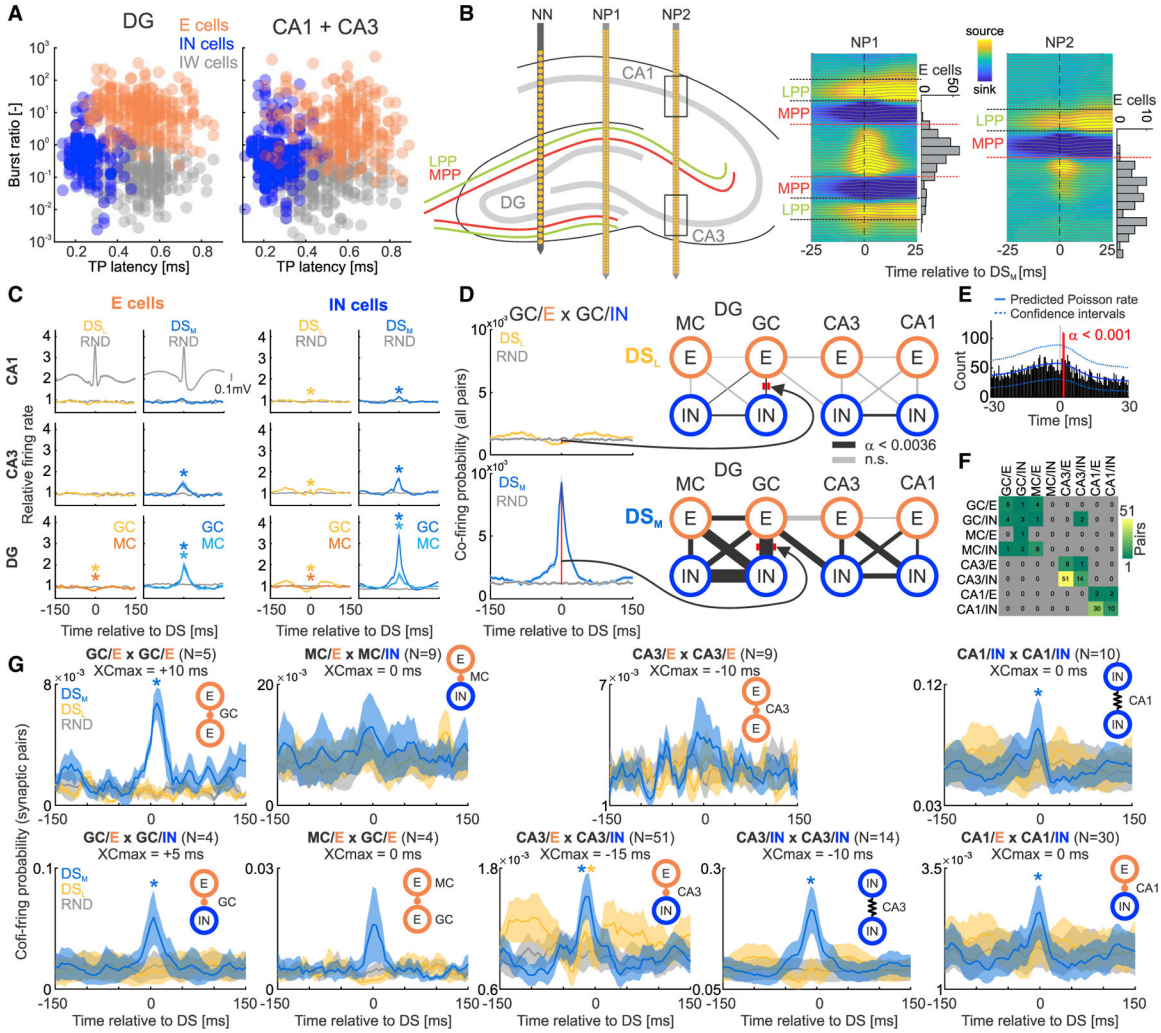

Figure 6. DS_M increases action potential discharge and cofiring in DG, CA3, and CA1 networks

(A) Unitary action potentials were classified as being from excitatory cells (Es), narrow-waveform interneurons (IN), and wide-waveform interneurons (IW) using the K-means algorithm on the DG-localized (left), and separately, the CA3- and CA1-localized datasets (right).

(B) Schematic mouse hippocampus (left) with medial placement of Neuronexus linear electrode array (NN) for detection of DS events and 2 example lateral placements of Neuropixels probes, NP1 proximal to DG and NP2 proximal to CA3. Distinctive DS_M-triggered average CSDs distinguish DG and CA3 localization. Rectangles along NP2 show CA1 and CA3 unit localization (Figure S5A). Corresponding depth distributions of putative excitatory cells are shown on the right of CSDs. Dotted lines: DG borders of granule cell (red) and outer molecular (black) layers.

(C) Normalized firing rates of CA1 (top), CA3 (center), and DG (bottom) units during DS_L (left) and DS_M (right) and random (gray) events. DS contaminated by SWR events were excluded. DS averages in gray.

(D) Representative cofiring probability of pairs of GC principal cells (GC/Es) and proximal narrow waveform interneurons (GC/IN) around DS_L (left, top, yellow) and DS_M (left,

Author Manuscript Author Manuscript Author Manuscript Author Manuscript

bottom, blue) and random (gray) events. Ratio of cofiring probability during DS events and random times is represented as line thickness (right) in a DG→CA3→CA1 network schematic; black connections significantly differ from random times, while gray connections do not after Bonferroni corrections (Table S1).

(E) Identification of a putative monosynaptic connection using enhanced spike-transmission strength in spike-time cross-correlogram. Solid blue line is expected cross-correlogram from Poisson model, dotted blue lines indicate confidence intervals, and red bins mark significant deviations from the model.

(F) Summary matrix of counts of all identified monosynaptic pairs.

(G) Cofiring probability during DS_L (yellow), DS_M (blue), and random times (gray) in identified pairs with monosynaptic spike-transmission statistics. The title of each subplot shows the time of maximum cross-correlation relative to DS, when statistics were computed. Stars mark significant deviations from random times.

Averages ± SEM are plotted.

Author Manuscript Author Manuscript Author Manuscript Author Manuscript

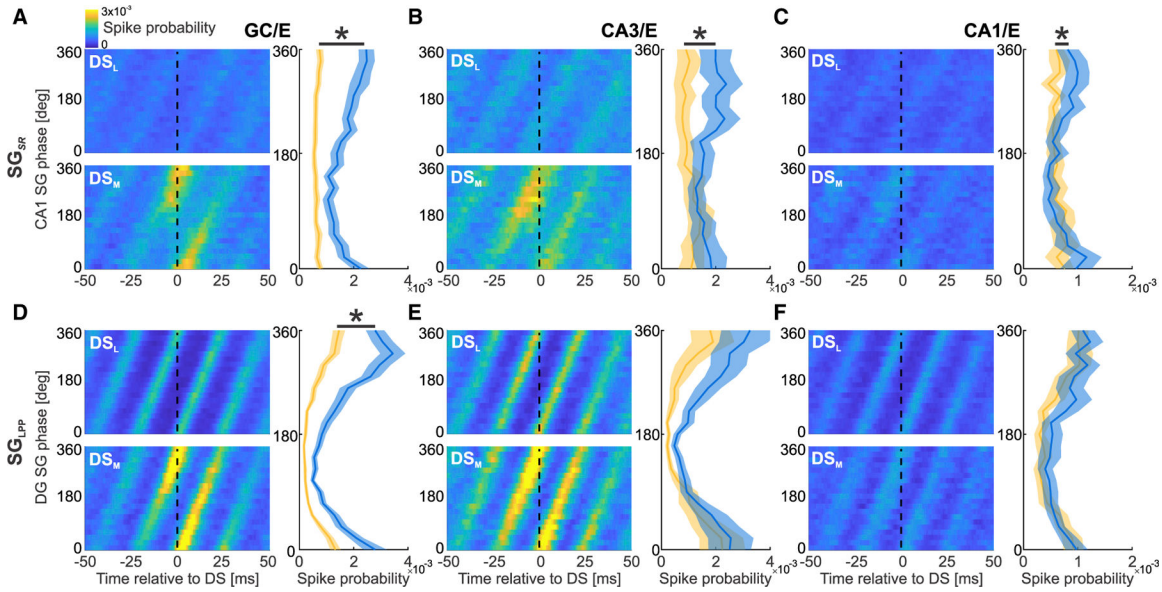

Figure 7. DS_M phase synchronizes discharge of GC, CA3, and CA1 cells through SG_{SR}

(A) Average discharge probability of a granule cell relative to DS times (x axis; DS_L top; DS_M bottom) and SG_{SR} phase (y axis). Data averaged across cells for DS_L (yellow) and DS_M (blue) at DS peak (T = 0) shown at right. Stars mark a significant difference between the DS_L and DS_M phase distributions.

(B and C) Same as (A), but for (B) CA3 and (C) CA1 Es.

(D) Same as (A), but for SG_{LPP} gamma phase (y axis).

(E and F) Same as (D), but for (E) CA3 and (F) CA1 Es.

Author Manuscript Author Manuscript Author Manuscript Author Manuscript

KEY RESOURCES TABLE

REAGENT or RESOURCE	SOURCE	IDENTIFIER
Deposited data		
LFP, position and spike-time data	This paper	https://doi.gin.g-node.org/10.12751/g-node.o1ho0y
Experimental models: organisms/strains		
Mice with a mixed C57BL/6J background	Jackson Laboratory	https://www.jax.org/strain/000664
Software and algorithms		
MATLAB	Mathworks	https://www.mathworks.com
JMP	JMP	https://www.jmp.com/en_us/home.geo.html
FastICA	Aalto University	https://research.ics.aalto.fi/ica/fastica/
CSDPlotter	GitHub	https://github.com/espenhgn/CSDplotter
Custom MATLAB analysis code	This paper	https://doi.gin.g-node.org/10.12751/g-node.o1ho0y